Multibody System Dynamics
https://doi.org/10.1007/s11044-024-10019-z

RESEARCH

Balancing riderless electric scooters at zero speed in the presence of a feedback delay

Hanna Zsofia Horvath[1] · **Denes Takacs**[1,2]

Received: 31 August 2023 / Accepted: 29 July 2024

Abstract
The nonlinear dynamics of electric scooters are investigated using a spatial mechanical model. The equations of motion are derived with the help of Kane's method. Two control algorithms are designed in order to balance the e-scooter in a vertical position at zero forward speed. Hierarchical, linear state feedback controllers with feedback delay are considered. In the case of a delay-free controller, the linear stability properties are analyzed analytically, with the help of the Routh–Hurwitz criteria. The linear stability charts of the delayed controllers are constructed with the help of the D-subdivision method and semi-discretization. The control gains of the controllers are optimized with respect to the robustness against perturbations. The effects of the feedback delay of the controllers, the rake angle, the trail, and the center of gravity of the handlebar on the linear stability are shown. The performance of the control algorithms is verified by means of numerical simulations.

Keywords E-scooter · Multibody system · Kane's method · Control with steering · Control with driving · Nonlinear simulations

1 Introduction

Single-track vehicles such as motorcycles, bicycles, and electric scooters (so-called e-scooters) became very popular in road transportation in the last decades. Vehicle stability, especially the lateral dynamics of such multibody systems is of utmost importance. Although motorcycles, bicycles, and e-scooters can be modeled with the same mechanical model, they have different geometric features and characteristics.

On the one hand, the dynamics of motorcycles [5, 22, 28, 30–32, 34] and bicycles [2, 6, 11, 13, 14, 17, 20, 25, 29, 35, 36, 40] have been investigated for a long time. Therefore, experts in the field know a lot about the dynamic properties of these vehicles, both in theoretical and practical aspects. On the other hand, the complex structure of the geometric and kinematic constraints of the spatial mechanical model provides a set of nonlinear differential equations that cannot be managed analytically. Hence, most of the literature focuses

✉ H.Z. Horvath
hanna.horvath@mm.bme.hu

[1] Department of Applied Mechanics, Faculty of Mechanical Engineering, Budapest University of Technology and Economics, Budapest, Hungary

[2] HUN-REN–BME Dynamics of Machines Research Group, Budapest, Hungary

Published online: 12 August 2024

on the semi-analytical and/or numerical stability analysis, and often small vibrations are investigated (i.e., linear stability analysis is carried out).

The benchmark model of bicycles with constant forward velocity has been introduced in [17]. It was shown that the bicycle is self-stable within a velocity range, i.e., between the so-called weave speed and the capsize speed. For a long time, it was believed that this self-stability is correlated to gyroscopic and caster effects. However, based on [14], neither the gyroscopic precession of the front wheel nor a positive trail is necessary for self-stability. In contrast, geometric properties like the front-assembly mass distribution or the rake angle of the bicycle play a relevant role in self-stability. Besides the investigation of the dynamics of uncontrolled bicycles, control strategies for path-tracking [6], fuzzy control for equilibrium and roll angle tracking [4], human control of a bicycle considering reaction time [16], and the optimal handling of a bicycle [21] have also been studied recently.

As a possible solution for the first and last mile problem in our modern road transport, e-scooters [12, 23] and electric unicycles [3] became fairly popular. The growing number of sharing companies enabled the spread of such micro-mobility vehicles. As a public transport vehicle, e-scooters are easily available in many cities. In addition, they are relatively small-sized, compact, and foldable. Since they are electric, they are considered green and environmentally conscious. In contrast, they are often unstable in the legislated riding velocity range [23] and many e-scooter drivers are inexperienced. Therefore, plenty of accidents happen due to falling off the e-scooter and/or collisions with other vehicles. In addition, e-scooters are often scattered in the streets, since many people do not leave them in the docking areas. With a proper design and profound knowledge of the dynamic behavior of such multibody systems, the number of accidents could be reduced to a noticeable extent.

Our study focuses on the stability of a riderless, self-driving e-scooter, which can balance itself in a vertical position. We propose that self-driving e-scooter at low speeds may be a useful option for e-scooter sharing companies in the future to transport e-scooters to docking stations or designated parking areas. As a first step, the balancing problem at zero forward speed is analyzed in this study, which is a very complex task even for professional bicycle riders. Besides linear stability analysis of the closed-loop system, the nonlinear governing equations are also derived and nonlinear numerical simulations are performed. Nevertheless, the time delay in the control algorithm is also taken into account.

The rest of the paper is organized as follows. The mechanical model, the geometric and kinematic constraints, and the derivation of the nonlinear governing equations are summarized in Sect. 2. Two linear feedback controllers with feedback delay are designed, linear stability charts are constructed, and the effect of several parameters on the linear stability properties are shown in Sect. 3. The control algorithms are verified by means of nonlinear numerical simulations in Sect. 4. Conclusions are drawn in Sect. 5.

2 Modeling

2.1 Mechanical model

In our analysis, we consider an electric scooter rolling on the rigid flat ground. To describe the motion of this vehicle, we use a spatial mechanical model that is based on the Whipple bicycle model [39]. Namely, the multibody system consists of four rigid bodies (see Fig. 1(a)): the front and the rear wheels, the body (i.e., the frame), and the handlebar (i.e., the handlebar and fork assembly). Subscripts f, r, b and h refer to these rigid bodies, respectively. All four rigid bodies have six degrees of freedom (DoF) without constraints, leading

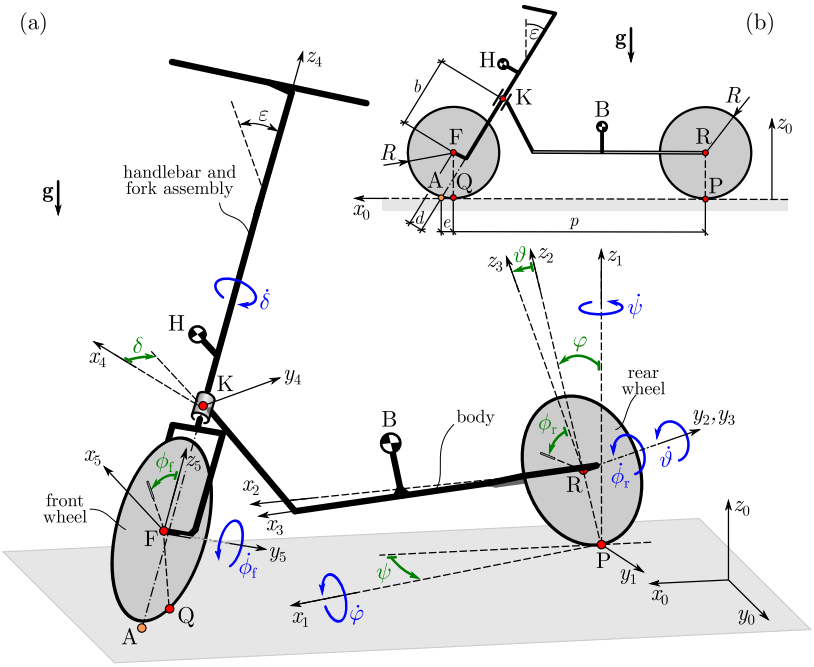

Fig. 1 The spatial model of an electric scooter (e-scooter). (a) Axonometric view with the generalized coordinates, angular velocities and reference frames. (b) Side view for $\psi = 0$, $\varphi = 0$, $\vartheta = 0$ and $\delta = 0$ with the geometric parameters

to 24 DoF altogether. Each of the three hinges between the bodies constrains three translational and two rotational DoF. This means that the e-scooter has $24 - 3 \cdot 5 = 9$ DoF without the consideration of the wheel-ground contacts.

The geometric parameters of the e-scooter can be seen in Fig. 1(b) in the nominal position and orientation (the center planes of the body and wheels are vertical). Let us denote the center points of the rigid wheels with F and R, and their single contact points with Q and P, respectively. The distance between the front and the rear wheel contact points (i.e., the wheelbase) is denoted by p. The trail e is the distance between the intersection point A of the steering axis and the ground and the front contact point Q. A positive value of e refers to towed front wheel (i.e., A is ahead Q), while a negative value of e corresponds to pushed front wheel (i.e., A is behind Q). Note that in general cases, the trail is positive ($e > 0$), and a negative trail ($e < 0$) is used only in special designs. The rake angle ε (also called steer tilt or steering axis angle, see [12, 17]) is the angle between the vertical direction and the steering axis.

In our model, we assume that the centers of gravity of the wheels are at the center points F and R, respectively, and both wheels have the same radius R. However, we consider different mass and mass moment of inertia parameters for the wheels. Namely, the front wheel (together with the hub motor in our case) has mass m_f and mass moment of inertia tensor $\mathbf{J}_\mathrm{F}$, and the rear wheel has mass m_r and mass moment of inertia tensor $\mathbf{J}_\mathrm{R}$. The mass of the body is m_b and the mass moment of inertia tensor about its center of mass B is denoted by $\mathbf{J}_\mathrm{B}$. The handlebar and the fork assembly have mass m_h and mass moment of inertia tensor $\mathbf{J}_\mathrm{H}$ about its center of mass H. The assembly is joined to the body at the kingpin K. The

fork length and fork offset are referred to b and d, respectively. The fork offset d can be expressed as a function of the wheel radius, the trail, and the rake angle:

$$d = R \sin \varepsilon - e \cos \varepsilon \,. \tag{1}$$

The spatial position of the multibody system consisting of the four rigid bodies can be described by the X, Y and Z coordinates of point R, the yaw angle ψ, the lean angle φ, the steering angle δ, the pitch angle ϑ, and the rotational angles ϕ_f and ϕ_r of the front and the rear wheels around their own axes. Up to this point, the constraints related to the wheel-ground contacts have not yet been taken into account; they are detailed in a later section.

In order to balance the e-scooter, we design two control algorithms. In the case of control with steering, we try to balance the vehicle by applying internal steering torque M^s on the handlebar. In the case of control with driving, we turn the front wheel into a $\pi/2$ steering angle position and apply internal driving torque M^d on the front wheel.

2.2 Coordinate frames

In our study, we define six frames. The ground-fixed global reference frame is referred to $\mathcal{F}_0$ with the coordinate system (x_0, y_0, z_0), with bases $\mathbf{i}_0$, $\mathbf{j}_0$ and $\mathbf{k}_0$. The other five reference frames $\mathcal{F}_k$ are provided by means of subsequent angular rotations: with the yaw angle ψ about the z_0-axis, with the lean angle φ about the x_1-axis, with the pitch angle ϑ about the y_2-axis. Hence, (x_3, y_3, z_3), denoted by $\mathcal{F}_3$, is the body-fixed reference frame. To get the reference frame of the handlebar and fork assembly, further two rotations are necessary: with the rake angle ε about the y_3-axis in the negative direction and with the steering angle δ about the z_4-axis. This provides the coordinate system (x_5, y_5, z_5) denoted by $\mathcal{F}_5$. The rotations (i.e., the transformation between the reference frames) can be expressed with rotational/transformation matrices:

$$\mathbf{T}_{0,1} = \begin{bmatrix} \cos\psi & -\sin\psi & 0 \\ \sin\psi & \cos\psi & 0 \\ 0 & 0 & 1 \end{bmatrix}, \quad \mathbf{T}_{1,2} = \begin{bmatrix} 1 & 0 & 0 \\ 0 & \cos\varphi & -\sin\varphi \\ 0 & \sin\varphi & \cos\varphi \end{bmatrix}, \tag{2}$$

$$\mathbf{T}_{2,3} = \begin{bmatrix} \cos\vartheta & 0 & \sin\vartheta \\ 0 & 1 & 0 \\ -\sin\vartheta & 0 & \cos\vartheta \end{bmatrix}, \quad \mathbf{T}_{3,4} = \begin{bmatrix} \cos\varepsilon & 0 & -\sin\varepsilon \\ 0 & 1 & 0 \\ \sin\varepsilon & 0 & \cos\varepsilon \end{bmatrix}, \tag{3}$$

$$\mathbf{T}_{4,5} = \begin{bmatrix} \cos\delta & -\sin\delta & 0 \\ \sin\delta & \cos\delta & 0 \\ 0 & 0 & 1 \end{bmatrix}. \tag{4}$$

With the help of these rotational matrices, a general expression for the transform of an arbitrary vector $\mathbf{r}$ can be derived as

$$\mathbf{r}_{\mathcal{F}_i} = \mathbf{T}_{i,j} \cdot \mathbf{r}_{\mathcal{F}_j} \,, \tag{5}$$

thus, the transform of a matrix $\mathbf{J}$ can be expressed as

$$\mathbf{J}_{\mathcal{F}_i} = \mathbf{T}_{i,j} \cdot \mathbf{J}_{\mathcal{F}_j} \cdot \mathbf{T}_{i,j}^\mathrm{T} \,, \tag{6}$$

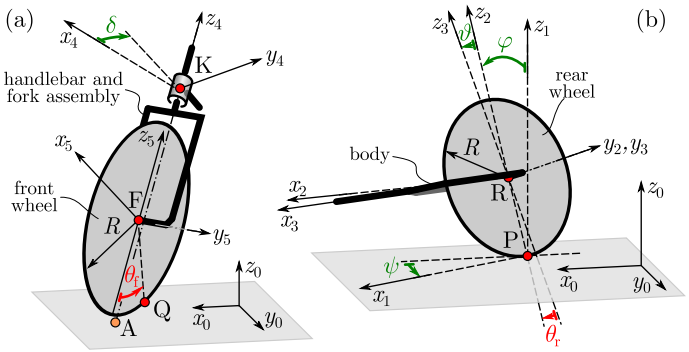

Fig. 2 Positions of the wheels' contact points in the wheel-aligned reference frames

where $\mathbf{T}_{i,j}^{\mathrm{T}}$ is the transpose of matrix $\mathbf{T}_{i,j}$. The transformation between coordinate frames n and m is a series of transformations:

$$\mathbf{T}_{n,m} = \prod_{j=n}^{m-1} \mathbf{T}_{j,j+1}\,, \tag{7}$$

where $n < m$.

2.3 Kinematics

In order to assume the wheel-ground contacts in the mechanical model, we summarize the kinematics (geometrical relations, velocities and accelerations) of the e-scooter in this section. Unfortunately, the mechanical model provides complicated formulas thanks to the complex geometrical relations. Hence, at some points of the derivation, we limited our summary to show the basic ideas of the calculations and we do not spell out the final formulas.

Let us start with the positions of the wheel-ground contact points. When the front wheel of the e-scooter is steered about the tilted (in case of non-zero rake angle) kingpin, the body is pitching and as a consequence, the relative positions of the front and rear wheels' contact points (Q and P) are changing in frames $\mathcal{F}_5$ and $\mathcal{F}_3$, respectively. Since these contact points are located along the circumference of the wheels, the position vectors between the center points of the wheels (F and R) and the contact points (Q and P) are

$$\mathbf{r}_{\mathrm{FQ}} = \begin{bmatrix} -R\sin\theta_{\mathrm{f}} \\ 0 \\ -R\cos\theta_{\mathrm{f}} \end{bmatrix}_{\mathcal{F}_5}, \quad \mathbf{r}_{\mathrm{RP}} = \begin{bmatrix} R\sin\theta_{\mathrm{r}} \\ 0 \\ -R\cos\theta_{\mathrm{r}} \end{bmatrix}_{\mathcal{F}_3}, \tag{8}$$

respectively. The angles θ_{f} and θ_{r} are shown in Fig. 2. Using the fact, that the z_0 coordinates of the contact points are minimal, one can determine these angles in the following form:

$$\theta_{\mathrm{f}} = \arctan\left(\frac{\cos\delta\cos\varphi\sin(\varepsilon-\vartheta)+\sin\delta\sin\varphi}{\cos\varphi\cos(\varepsilon-\vartheta)}\right), \quad \theta_{\mathrm{r}} = \vartheta\,. \tag{9}$$

Thus, the angle related to the front wheel has a complicated nonlinear dependence on the lean, steering, pitch, and rake angles. On the contrary, the situation on the rear wheel is simple: the position of the contact point can be parameterized by the pitch angle.

To determine the velocities of the contact points, one has to define the state of velocity of the rigid bodies included in the model. The angular velocity vector of the body can be represented in frame $\mathcal{F}_0$ as

$$\begin{aligned}\boldsymbol{\omega}_\mathrm{b} = \dot{\psi}\begin{bmatrix}0\\0\\1\end{bmatrix}_{\mathcal{F}_0} + \dot{\varphi}\,\mathbf{T}_{0,1}\begin{bmatrix}1\\0\\0\end{bmatrix}_{\mathcal{F}_1} + \dot{\vartheta}\,\mathbf{T}_{0,2}\begin{bmatrix}0\\1\\0\end{bmatrix}_{\mathcal{F}_2} = \\ = \begin{bmatrix}\cos\psi\dot{\varphi} - \sin\psi\cos\varphi\dot{\vartheta}\\ \sin\psi\dot{\varphi} + \cos\psi\cos\varphi\dot{\vartheta}\\ \dot{\psi} + \sin\varphi\dot{\vartheta}\end{bmatrix}_{\mathcal{F}_0}.\end{aligned} \tag{10}$$

Similarly, the angular velocity vector of the handlebar can be calculated as

$$\boldsymbol{\omega}_\mathrm{h} = \boldsymbol{\omega}_\mathrm{b} + \dot{\delta}\,\mathbf{T}_{0,5}\begin{bmatrix}0\\0\\1\end{bmatrix}_{\mathcal{F}_5}. \tag{11}$$

The angular velocity vectors of the front and the rear wheels are determined by

$$\boldsymbol{\omega}_\mathrm{f} = \boldsymbol{\omega}_\mathrm{h} + \dot{\phi}_\mathrm{f}\,\mathbf{T}_{0,5}\begin{bmatrix}0\\1\\0\end{bmatrix}_{\mathcal{F}_5}, \quad \boldsymbol{\omega}_\mathrm{r} = \boldsymbol{\omega}_\mathrm{b} + \dot{\phi}_\mathrm{r}\,\mathbf{T}_{0,3}\begin{bmatrix}0\\1\\0\end{bmatrix}_{\mathcal{F}_3}. \tag{12}$$

The velocity of the center point of the rear wheel R can be calculated as the time derivative of the position vector $\mathbf{r}_\mathrm{R}$ in the ground-fixed $\mathcal{F}_0$ reference frame:

$$\mathbf{v}_\mathrm{R} = \dot{\mathbf{r}}_\mathrm{R}, \tag{13}$$

where

$$\mathbf{r}_\mathrm{R} = \begin{bmatrix}X & Y & Z\end{bmatrix}^\mathrm{T}_{\mathcal{F}_0}. \tag{14}$$

The velocities of the kingpin (K) and the centers of gravity (B, H, F) of the other three rigid bodies can be expressed by means of transport formulas as

$$\mathbf{v}_\mathrm{K} = \mathbf{v}_\mathrm{R} + \boldsymbol{\omega}_\mathrm{b} \times \mathbf{r}_\mathrm{RK}, \tag{15}$$

$$\mathbf{v}_\mathrm{B} = \mathbf{v}_\mathrm{R} + \boldsymbol{\omega}_\mathrm{b} \times \mathbf{r}_\mathrm{RB}, \tag{16}$$

$$\mathbf{v}_\mathrm{H} = \mathbf{v}_\mathrm{K} + \boldsymbol{\omega}_\mathrm{h} \times \mathbf{r}_\mathrm{KH}, \tag{17}$$

$$\mathbf{v}_\mathrm{F} = \mathbf{v}_\mathrm{K} + \boldsymbol{\omega}_\mathrm{h} \times \mathbf{r}_\mathrm{KF}. \tag{18}$$

The components of the necessary position vectors in Eqs. (15)-(18) can be given with the geometric parameters and by defining the centers of gravity of the body and the handlebar. Based on Fig. 1(b), the position vector to the kingpin K can be expressed as

$$\mathbf{r}_\mathrm{RK} = \begin{bmatrix}p - b\sin\varepsilon - d\cos\varepsilon\\ 0\\ b\cos\varepsilon - d\sin\varepsilon\end{bmatrix}_{\mathcal{F}_3}, \tag{19}$$

and the position vector from the kingpin K to the center point of the front wheel F can be given in the handlebar-fixed reference frame $\mathcal{F}_5$ as

$$\mathbf{r}_{\mathrm{KF}} = \begin{bmatrix} d & 0 & -b \end{bmatrix}^{\mathrm{T}}_{\mathcal{F}_5} . \tag{20}$$

We assume that the center of gravity of the body is known and can be given in the body-fixed reference frame $\mathcal{F}_3$ as

$$\mathbf{r}_{\mathrm{RB}} = \begin{bmatrix} x_{\mathrm{RB}} & 0 & z_{\mathrm{RB}} \end{bmatrix}^{\mathrm{T}}_{\mathcal{F}_3} . \tag{21}$$

The center of gravity of the handlebar is also known and can be given in the handlebar-fixed reference frame $\mathcal{F}_5$ as

$$\mathbf{r}_{\mathrm{KH}} = \begin{bmatrix} x_{\mathrm{KH}} & 0 & z_{\mathrm{KH}} \end{bmatrix}^{\mathrm{T}}_{\mathcal{F}_5} . \tag{22}$$

Using the above-derived formulas, one can calculate the velocity vectors of the front and the rear contact points:

$$\mathbf{v}_{\mathrm{Q}} = \mathbf{v}_{\mathrm{F}} + \boldsymbol{\omega}_{\mathrm{f}} \times \mathbf{r}_{\mathrm{FQ}} , \tag{23}$$

$$\mathbf{v}_{\mathrm{P}} = \mathbf{v}_{\mathrm{R}} + \boldsymbol{\omega}_{\mathrm{r}} \times \mathbf{r}_{\mathrm{RP}} . \tag{24}$$

In the next subsection, these formulas are used for the definitions of the kinematic constraints of rolling.

2.4 Constraints related to the wheel-ground contacts

In our investigation, the front and the rear wheels are attached to the ground, leading to two additional geometric constraints in the system. Namely, the vertical components (r_{Q}^{z0} and r_{P}^{z0}) of the front and the rear contact points (Q and P) in the ground-fixed reference frame $\mathcal{F}_0$ are zeros:

$$\mathbf{r}_{\mathrm{Q}} \cdot \mathbf{k}_0 =: r_{\mathrm{Q}}^{z0} = 0 , \tag{25}$$

$$\mathbf{r}_{\mathrm{P}} \cdot \mathbf{k}_0 =: r_{\mathrm{P}}^{z0} = 0 . \tag{26}$$

These nonlinear algebraic equations reduce the number of generalized coordinates that are required to describe the motion of the e-scooter. Intuitively, one can use Eq. (26) to eliminate coordinate Z as

$$Z = R \cos \varphi , \tag{27}$$

and using this in Eq. (25) allows us to suppress the pitch angle ϑ as a function of the lean and the steering angles. Namely, Eq. (25) provides a quartic equation for $\sin \vartheta$, which can be analytically solved, as shown in [24, 26, 40]. Since this analytical solution can make further calculations very complicated, the so-called dynamic inclusion is often used, see [24].

The constraint equation (25) is manifested by the surface in Fig. 3(a) for a parameter setup based on the literature [12] (see the parameter values in Table 1). As it can be seen, the pitch angle is quite small even if the handlebar is steered extremely (i.e., $\delta = \pm\pi/2$) and the lean angle is moderate, which is also shown in [20].

We assume that the wheels roll purely on the flat ground. This assumption manifests in kinematic constraining equations for the front and rear contact points. Altogether, four

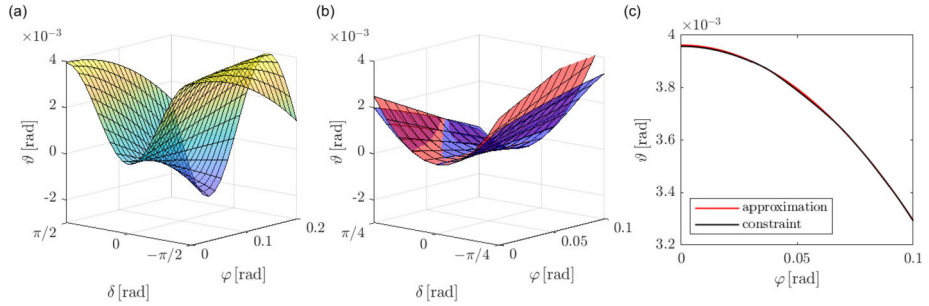

Fig. 3 (a) The surface corresponding to the geometric constraint of Eq. (25), (b) the exact and the approximate surfaces (corresponding to Eqs. (25) and (47), respectively) representing the relation within the lean, the steering and the pitch angles in case of control with steering, (c) the exact and the approximate curves (corresponding to Eqs. (25) and (68), respectively) representing the relation within the lean and the pitch angles in case of control with driving (color figure online)

scalar kinematic constraining equations can be formulated for the two wheels (the velocity components in the ground plane are zeros):

$$\begin{aligned} \mathbf{v}_{\mathrm{Q}} \cdot \mathbf{i}_0 =: v_{\mathrm{Q}}^{x_0} = 0\,, \quad \mathbf{v}_{\mathrm{Q}} \cdot \mathbf{j}_0 =: v_{\mathrm{Q}}^{y_0} = 0\,, \\ \mathbf{v}_{\mathrm{P}} \cdot \mathbf{i}_0 =: v_{\mathrm{P}}^{x_0} = 0\,, \quad \mathbf{v}_{\mathrm{P}} \cdot \mathbf{j}_0 =: v_{\mathrm{P}}^{y_0} = 0\,. \end{aligned} \tag{28}$$

Thus, the system is non-holonomic and the derivation of the governing equations needs special attention, as also discussed in [27], where the Appellian approach is in focus. Here, we use Kane's method [10], which was developed later using the same concept of pseudo velocities.

2.5 Kane's method

As formerly explained, each of the three hinges between the rigid bodies constrains five DoF and the wheel-ground contacts lead to two additional geometric constraints. Therefore, we have $3 \cdot 5 + 2 = 17$ geometric constraint equations. This means that the configuration space is $24 - 17 = 7$ dimensional, i.e., one has to choose seven generalized coordinates. Let us choose the coordinates X and Y of the center point R of the rear wheel, the yaw angle ψ, the lean angle φ, the steering angle δ, and the rotational angles ϕ_{f} and ϕ_{r} of the front and the rear wheels around their own axes, see Fig. 1. Thus, the vector of generalized coordinates is

$$\mathbf{q} = \begin{bmatrix} X & Y & \psi & \varphi & \delta & \phi_{\mathrm{f}} & \phi_{\mathrm{r}} \end{bmatrix}^{\mathrm{T}}. \tag{29}$$

The kinematic constraining equations formulated in Eq. (28) can be written as

$$\mathbf{A}\dot{\mathbf{q}} = \mathbf{0}\,, \tag{30}$$

where the coefficient matrix $\mathbf{A}$ is

$$\mathbf{A} = \begin{bmatrix} 1 & 0 & A_{13} & A_{14} & A_{15} & A_{16} & 0 \\ 0 & 1 & A_{23} & A_{24} & A_{25} & A_{26} & 0 \\ 1 & 0 & A_{33} & A_{34} & A_{35} & 0 & A_{37} \\ 0 & 1 & A_{43} & A_{44} & A_{45} & 0 & A_{47} \end{bmatrix}. \tag{31}$$

Using Kane's method [10], one has to choose so-called pseudo velocities. On the one hand, this is an intuitive choice; on the other hand, a unique system description must be provided. In addition, the complexity of the governing equations depends significantly on this choice. The number of pseudo velocities is equal to the difference between the number of the generalized coordinates and the number of kinematic constraints, i.e., $7-4=3$ in this study. Let us choose the lean rate $\dot{\varphi}$, the steering rate $\dot{\delta}$ and the angular velocity of the front wheel $\dot{\phi}_\mathrm{f}$ as pseudo velocities. That is, the vector of pseudo velocities is

$$\boldsymbol{\sigma} = \begin{bmatrix} \sigma_1 & \sigma_2 & \sigma_3 \end{bmatrix}^\mathrm{T} := \begin{bmatrix} \dot{\varphi} & \dot{\delta} & \dot{\phi}_\mathrm{f} \end{bmatrix}^\mathrm{T} . \tag{32}$$

This can be written in matrix form as

$$\mathbf{B}\dot{\mathbf{q}} = \boldsymbol{\sigma} , \tag{33}$$

where the coefficient matrix $\mathbf{B}$ has the form

$$\mathbf{B} = \begin{bmatrix} 0 & 0 & 0 & 1 & 0 & 0 & 0 \\ 0 & 0 & 0 & 0 & 1 & 0 & 0 \\ 0 & 0 & 0 & 0 & 0 & 1 & 0 \end{bmatrix} . \tag{34}$$

The kinematic constraints and the definitions of the pseudo velocities form a system of linear algebraic equations:

$$\begin{bmatrix} \mathbf{A} \\ \mathbf{B} \end{bmatrix} \begin{bmatrix} \dot{\mathbf{q}} \end{bmatrix} = \begin{bmatrix} \mathbf{0} \\ \boldsymbol{\sigma} \end{bmatrix} , \tag{35}$$

namely

$$\underbrace{\begin{bmatrix} 1 & 0 & A_{13} & A_{14} & A_{15} & A_{16} & 0 \\ 0 & 1 & A_{23} & A_{24} & A_{25} & A_{26} & 0 \\ 1 & 0 & A_{33} & A_{34} & A_{35} & 0 & A_{37} \\ 0 & 1 & A_{43} & A_{44} & A_{45} & 0 & A_{47} \\ 0 & 0 & 0 & 1 & 0 & 0 & 0 \\ 0 & 0 & 0 & 0 & 1 & 0 & 0 \\ 0 & 0 & 0 & 0 & 0 & 1 & 0 \end{bmatrix}}_{=:\mathbf{C}} \begin{bmatrix} \dot{X} \\ \dot{Y} \\ \dot{\psi} \\ \dot{\varphi} \\ \dot{\delta} \\ \dot{\phi}_\mathrm{f} \\ \dot{\phi}_\mathrm{r} \end{bmatrix} = \begin{bmatrix} 0 \\ 0 \\ 0 \\ 0 \\ \sigma_1 \\ \sigma_2 \\ \sigma_3 \end{bmatrix} . \tag{36}$$

In order to have a unique solution for the generalized velocities $\dot{q}_k$, the coefficient matrix $\mathbf{C}$ has to be non-singular, i.e., $\det \mathbf{C} \neq 0$. The pseudo velocities are chosen so that this criterion is fulfilled.

The Kane equations can be written as

$$F_j + F_j^* = 0 , \quad j = 1, 2, 3 , \tag{37}$$

where

$$F_j = \sum_{i \in \{\text{bodies}\}} \left(\mathbf{F}_i \cdot \frac{\partial \mathbf{v}_i}{\partial \sigma_j} + \mathbf{M}_i \cdot \frac{\partial \boldsymbol{\omega}_i}{\partial \sigma_j} \right) , \tag{38}$$

$$F_j^* = - \sum_{i \in \{\text{bodies}\}} \left(m_i \mathbf{a}_i \cdot \frac{\partial \mathbf{v}_i}{\partial \sigma_j} + (\mathbf{J}_i \boldsymbol{\varepsilon}_i + \boldsymbol{\omega}_i \times (\mathbf{J}_i \boldsymbol{\omega}_i)) \cdot \frac{\partial \boldsymbol{\omega}_i}{\partial \sigma_j} \right) . \tag{39}$$

Here, $\mathbf{a}_i = \dot{\mathbf{v}}_i$ are accelerations of the centers of gravity (B, H, F, R), $\boldsymbol{\varepsilon}_i = \dot{\boldsymbol{\omega}}_i$ are the angular accelerations of the bodies, $\mathbf{F}_i$ are the active forces and $\mathbf{M}_i$ are the torques on body i. The active forces on the rigid bodies are the gravitational forces:

$$\mathbf{F}_i = \begin{bmatrix} 0 & 0 & -m_i g \end{bmatrix}^{\mathrm{T}}_{\mathcal{F}_0}, \quad i \in \{\mathrm{b}, \mathrm{h}, \mathrm{f}, \mathrm{r}\}, \tag{40}$$

where g is the gravitational acceleration.

As a first approach, we try to balance the e-scooter by even applying internal steering torque M^{s} on the handlebar (control with steering) or by driving the front wheel with internal driving torque M^{d} (control with driving). Thus, the torques acting on the body, the handlebar, and the front wheel can be considered as

$$\mathbf{M}_{\mathrm{b}} = \begin{bmatrix} 0 \\ 0 \\ -M^{\mathrm{s}} \end{bmatrix}_{\mathcal{F}_5}, \quad \mathbf{M}_{\mathrm{h}} = \begin{bmatrix} 0 \\ -M^{\mathrm{d}} \\ M^{\mathrm{s}} \end{bmatrix}_{\mathcal{F}_5}, \quad \mathbf{M}_{\mathrm{f}} = \begin{bmatrix} 0 \\ M^{\mathrm{d}} \\ 0 \end{bmatrix}_{\mathcal{F}_5}. \tag{41}$$

By substituting all the above calculated kinematic quantities into Eq. (37), we get three first-order differential equations for the pseudo velocities. These together with the seven kinematic constraint equations expressed for the generalized velocities $\dot{q}_k$ from Eq. (30) form the system of nonlinear governing equations. Thus, altogether we have ten first-order differential equations, namely the state space is ten-dimensional. Or, as often referred to, the system is a 5 DoF dynamical system, see [27].

Due to the large number of parameters of the mechanical model and the complexity of the governing equations, only semi-analytical calculations can be performed. Namely, we consider parameter values for an existing e-scooter based on the data found in the literature [12]. The parameters with their notations, names, and values are given in Table 1. Note that the mass moment inertia values of the wheels about their rotational axes are smaller than the values about their other two axes, which is unconventional. However, we rely on the parameter values published in [12].

3 Control design

In order to balance the e-scooter in the vertical position, two different control strategies are proposed in our study. For the controller designs, we use reduced models, namely, we consider additional geometric constraints to reduce the complexity of the original model of Sect. 2.

3.1 Control with steering

First, we try to balance the e-scooter by using the steering mechanism, i.e., applying steering torque M^{s} on the handlebar. In the meantime, the rotational speed of the front wheel is kept at zero by considering $\dot{\phi}_{\mathrm{f}} = 0$, which leads to the geometric constraint $\phi_{\mathrm{f}} \equiv 0$. Consequently, the front wheel is fixed to the handlebar, and ϕ_{f} is not a generalized coordinate anymore. This can be considered for the kinematic constraints of rolling in Eq. (30) by deleting the sixth column of the coefficient matrix (31). Namely, only two pseudo velocities are required to describe the motion of the system. Let us use our former choice and keep $\sigma_1 = \dot{\varphi}$ and $\sigma_2 = \dot{\delta}$. Then, one can use the algorithm of Sect. 2.5 to determine the equations of motion of the reduced system, where the vector of state variables is

$$\mathbf{x} = \begin{bmatrix} \varphi & \delta \end{bmatrix}^{\mathrm{T}}. \tag{42}$$

Table 1 Parameters of the e-scooter

Notation	Parameter name	Value
p	wheelbase	0.829 m
e	trail	0.0281 m
ε	rake angle	14.2°
g	gravitational acceleration	9.81 m/s^2
R	wheel radius	0.111 m
front wheel		
m_f	mass	2.894 kg
$\mathbf{J}_\mathrm{F}$	mass moment of inertia in $\mathcal{F}_5$	$\begin{bmatrix} 0.01134 & 0 & 0 \\ 0 & 0.00628 & 0 \\ 0 & 0 & 0.01134 \end{bmatrix}$ kg m^2
rear wheel		
m_r	mass	1.136 kg
$\mathbf{J}_\mathrm{R}$	mass moment of inertia in $\mathcal{F}_3$	$\begin{bmatrix} 0.00536 & 0 & 0 \\ 0 & 0.0029 & 0 \\ 0 & 0 & 0.00536 \end{bmatrix}$ kg m^2
body		
m_b	mass	9.5 kg
$\mathbf{J}_\mathrm{B}$	mass moment of inertia in $\mathcal{F}_3$	$\begin{bmatrix} 0.1014 & 0 & -0.1074 \\ 0 & 0.4374 & 0 \\ -0.1074 & 0 & 0.3561 \end{bmatrix}$ kg m^2
$\mathbf{r}_\mathrm{RB}$	center of gravity	$[0.4314, 0, 0.0782]^\mathrm{T}$ m
handlebar		
m_h	mass	2.797 kg
$\mathbf{J}_\mathrm{H}$	mass moment of inertia in $\mathcal{F}_5$	$\begin{bmatrix} 0.341171 & 0 & 0.151596 \\ 0 & 0.4018 & 0 \\ 0.151596 & 0 & 0.0840292 \end{bmatrix}$ kg m^2
$\mathbf{r}_\mathrm{KH}$	center of gravity	$[0.01, 0, 0.2716]^\mathrm{T}$ m
b	length	0.2418 m
d	offset	0 m

For the linear stability of the rectilinear motion of the e-scooter, the nonlinear governing equations are linearized around the steady state $\mathbf{x}(t) \equiv \mathbf{x}_0$. We consider $\mathbf{x}_0 = \mathbf{0}$, namely

$$\varphi(t) \equiv \varphi_0 = 0\,, \tag{43}$$

$$\delta(t) \equiv \delta_0 = 0\,. \tag{44}$$

To simplify the derivation of the linearized equation of motion, one can use an approximation for the pitch angle instead of using the analytical solution of Eq. (25). Namely, the Taylor-series of the pitch angle reads

$$\vartheta = c_{00} + c_{10}\varphi + c_{01}\delta + c_{20}\varphi^2 + c_{02}\delta^2 + c_{11}\varphi\delta + \text{h.o.t.} \tag{45}$$

By taking the Taylor-series of the constraint equation (25), coefficients c_{ij} up to the second degree can be determined as

$$c_{00} = c_{10} = c_{01} = c_{20} = 0\,, \quad c_{02} = \frac{e}{4p}\sin 2\varepsilon\,, \quad c_{11} = -\frac{e}{p}\cos\varepsilon\,, \tag{46}$$

thus, the approximation of the pitch angle is obtained as

$$\vartheta \approx \frac{e}{4p}\delta^2 \sin 2\varepsilon - \frac{e}{p}\varphi\delta\cos\varepsilon\,. \tag{47}$$

In Fig. 3(b), the surface corresponding to the geometric constraint (25) is shown with blue color. The surface corresponding to the approximation (47) of ϑ is also plotted by red. As can be seen, the approximation is acceptable for small steering and lean angles. Moreover, this approximation provides the exact linearized equations of motion, since higher-order terms do not influence the linear part at the end of the derivation process.

Using the perturbation $\tilde{\mathbf{x}}(t) = \mathbf{x}(t) - \mathbf{x}_0$ around the steady state, the linearized equations of motion can be written as

$$\mathbf{M}\ddot{\tilde{\mathbf{x}}}(t) + \mathbf{K}\tilde{\mathbf{x}}(t) = \mathbf{Q}(t)\,, \tag{48}$$

where $\mathbf{M}$ is the mass matrix, $\mathbf{K}$ is the stiffness matrix, and $\mathbf{Q}(t) = \begin{bmatrix} 0 & M^{\mathrm{s}} \end{bmatrix}^{\mathrm{T}}$ is the vector of generalized forces. We also take into account the feedback delay of the controller by time delay τ. Of course, the above-described governing equations agree with the linear benchmark model in [17] for zero forward speed. The mass and the stiffness matrices are given numerically for the e-scooter of Table 1 in Appendix A.

As a first approach, we use a cascade controller. Namely, a higher-level controller calculates the desired steering angle as

$$\delta_{\mathrm{des}} = -K^{\mathrm{s}}_{\mathrm{p}\varphi}\varphi(t-\tau) - K^{\mathrm{s}}_{\mathrm{d}\varphi}\dot{\varphi}(t-\tau)\,, \tag{49}$$

where $K^{\mathrm{s}}_{\mathrm{p}\varphi}$ and $K^{\mathrm{s}}_{\mathrm{d}\varphi}$ are proportional gains for the lean angle and lean rate, respectively. This control law assumes that the sensors and actuators of an e-scooter have feedback delay τ, that is, actuation does not happen immediately. Namely, we only have information about the lean angle and the lean rate τ time after the exact time of the measurement of these quantities. Note that the accurate measurement of the lean angle is a complicated task, which may limit the use of our controller. However, nowadays, more and more micromobility vehicles such as electric unicycles and segways are on the roads, in which the tilt/lean angle control is solved similarly like in our study, see [3, 15]. With this control, we want to drive the steering angle to the desired value and the steering rate to zero. Therefore, the internal steering torque M^{s} is created by a lower-level control law as

$$M^{\mathrm{s}} = -K^{\mathrm{s}}_{\mathrm{p}\delta}\left(\delta(t) - \delta_{\mathrm{des}}\right) - K^{\mathrm{s}}_{\mathrm{d}\delta}\dot{\delta}(t)\,, \tag{50}$$

where $K^{\mathrm{s}}_{\mathrm{p}\delta}$ and $K^{\mathrm{s}}_{\mathrm{d}\delta}$ are proportional gains for the steering angle and steering rate, respectively. We assume that the time delay in the lower-level controller is negligible compared to the time delay in the higher-level controller. By applying the control laws described in Eqs. (49)-(50), the vector of generalized forces can be written as

$$\mathbf{Q}(t) = \mathbf{D}\dot{\tilde{\mathbf{x}}}(t) + \mathbf{P}\tilde{\mathbf{x}}(t) + \mathbf{D}_\tau\dot{\tilde{\mathbf{x}}}(t-\tau) + \mathbf{P}_\tau\tilde{\mathbf{x}}(t-\tau)\,, \tag{51}$$

where the matrices are

$$\mathbf{D} = \begin{bmatrix} 0 & 0 \\ 0 & -K^{\mathrm{s}}_{\mathrm{d}\delta} \end{bmatrix}, \quad \mathbf{P} = \begin{bmatrix} 0 & 0 \\ 0 & -K^{\mathrm{s}}_{\mathrm{p}\delta} \end{bmatrix}, \tag{52}$$

$$\mathbf{D}_\tau = \begin{bmatrix} 0 & 0 \\ -K^{\mathrm{s}}_{\mathrm{p}\delta} K^{\mathrm{s}}_{\mathrm{d}\varphi} & 0 \end{bmatrix}, \quad \mathbf{P}_\tau = \begin{bmatrix} 0 & 0 \\ -K^{\mathrm{s}}_{\mathrm{p}\delta} K^{\mathrm{s}}_{\mathrm{p}\varphi} & 0 \end{bmatrix}. \tag{53}$$

Hence, the linearized equations of motion can be written as

$$\mathbf{M}\ddot{\tilde{\mathbf{x}}}(t) - \mathbf{D}\dot{\tilde{\mathbf{x}}}(t) + (\mathbf{K} - \mathbf{P})\tilde{\mathbf{x}}(t) = \mathbf{D}_\tau \dot{\tilde{\mathbf{x}}}(t-\tau) + \mathbf{P}_\tau \tilde{\mathbf{x}}(t-\tau) \tag{54}$$

by arranging the non-delayed terms on the left-hand side and the delayed terms on the right-hand side.

In order to investigate the linear stability properties, one has to construct the characteristic equation of the system. By using the exponential trial solution $\tilde{\mathbf{x}}(t) = \mathbf{a}\,\mathrm{e}^{\lambda t}$ with characteristic exponent λ, we obtain the characteristic function of the system as

$$D_{\mathrm{char}}(\lambda) := \det\left(\mathbf{M}\lambda^2 - \mathbf{D}\lambda + (\mathbf{K} - \mathbf{P}) - (\mathbf{D}_\tau \lambda + \mathbf{P}_\tau)\,\mathrm{e}^{\lambda(-\tau)}\right). \tag{55}$$

3.1.1 Control with steering without time delay

As a first step, we consider zero feedback delay, i.e., $\tau = 0$. Thus, the characteristic function can be formulated as a simple polynomial:

$$\begin{aligned} D_{\mathrm{char}}(\lambda) &:= \det\left(\mathbf{M}\lambda^2 - \mathbf{D}\lambda + (\mathbf{K} - \mathbf{P}) - (\mathbf{D}_\tau \lambda + \mathbf{P}_\tau)\right) \\ &= b_0\lambda^4 + b_1\lambda^3 + b_2\lambda^2 + b_3\lambda + b_4\,. \end{aligned} \tag{56}$$

In this case, the stability boundaries can be analyzed semi-analytically. The stability criteria lead to complicated formulas, therefore they are not spelled out in the paper. The linear stability properties are shown for parameter values of Table 1. According to the Routh-Hurwitz stability criteria, all coefficients of the characteristic equation $D_{\mathrm{char}}(\lambda) = 0$ and the third principal minor $H_3 = b_3(b_1 b_2 - b_0 b_3) - b_1^2 b_4$ of the Hurwitz matrix have to be positive. It can be shown, that the coefficients of the characteristic equation are

$$b_0 = \det\mathbf{M}\,, \tag{57}$$

$$b_1 = 1.8061 K^{\mathrm{s}}_{\mathrm{d}\delta} - 0.035073 K^{\mathrm{s}}_{\mathrm{p}\delta} K^{\mathrm{s}}_{\mathrm{d}\varphi}\,, \tag{58}$$

$$b_2 = -5.8765 + 1.8061 K^{\mathrm{s}}_{\mathrm{p}\delta} - 0.035073 K^{\mathrm{s}}_{\mathrm{p}\varphi} K^{\mathrm{s}}_{\mathrm{p}\delta}\,, \tag{59}$$

$$b_3 = -38.790 K^{\mathrm{s}}_{\mathrm{d}\delta} - 3.0112 K^{\mathrm{s}}_{\mathrm{p}\delta} K^{\mathrm{s}}_{\mathrm{d}\varphi}\,, \tag{60}$$

$$b_4 = 19.585 - 38.790 K^{\mathrm{s}}_{\mathrm{p}\delta} - 3.0112 K^{\mathrm{s}}_{\mathrm{p}\varphi} K^{\mathrm{s}}_{\mathrm{p}\delta}\,. \tag{61}$$

In the linear stability chart of Fig. 4(a), the stability boundaries and the stable region are plotted in the plane of control gains $K^{\mathrm{s}}_{\mathrm{p}\varphi}$ and $K^{\mathrm{s}}_{\mathrm{d}\varphi}$. The lower-level control gains are fixed to $K^{\mathrm{s}}_{\mathrm{p}\delta} = 10$ Nm and $K^{\mathrm{s}}_{\mathrm{d}\delta} = -5$ Nms based on detailed analysis explained later in Sect. 3.1.3. The criterion $b_0 > 0$ is always fulfilled, since the determinant of the mass matrix is always positive. As can be seen in Fig. 4(a), the stability boundaries corresponding to $b_1 = 0$, $b_2 = 0$, $b_3 = 0$ and $b_4 = 0$ are horizontal and vertical lines for fixed parameters and lower-level control gains. In more details, the criteria $b_1 > 0$ and $b_3 > 0$ define a maximum

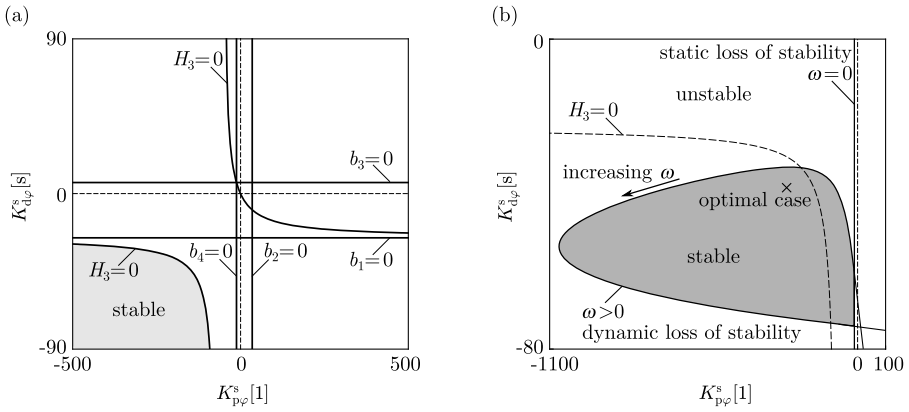

Fig. 4 Stability boundaries and the stable region for fixed parameters of Tab. 1 and fixed lower-level control gains: $K^s_{p\delta} = 10$ Nm and $K^s_{d\delta} = -5$ Nms. (a) For the non-delayed controller ($\tau = 0$) and (b) for feedback delay $\tau = 0.01$ s.

value for the derivative control gain $K^s_{d\varphi}$. Similarly, the criteria $b_2 > 0$ and $b_4 > 0$ define a maximum value for the proportional control gain $K^s_{p\varphi}$. All in all, the stable domain is restricted to a quarter-plane. Note, that coefficients (57)-(61) also allow the use of higher-level control gain setup from the first quadrant if the lower-level control gains are fixed to different values than in our study (see Sect. 3.1.3). The curve corresponding to $H_3 = 0$ is also marked in the figure. It can be shown, that the stable region is the gray shaded area.

Based on the linear stability chart of the zero delay case, one can choose the higher-level control gains appropriately. Namely, by choosing higher-level control gains from the stable region, the vertical position of the e-scooter is linearly stable. Let us now investigate the effect of the feedback delay on the stability.

3.1.2 Control with steering with time delay

For a delayed controller, i.e., $\tau > 0$, the characteristic equation $D_{\text{char}}(\lambda) = 0$ is transcendental due to the presence of the exponential terms related to the delay. However, the stability boundaries can be determined, where pure complex characteristic roots are situated on the imaginary axis of the complex plane. In our study, we use the D-subdivision method, thus, we substitute $\lambda = \mathrm{i}\omega$ into the characteristic equation and separate the real and imaginary parts:

$$\mathrm{Re}\left(D_{\text{char}}(\mathrm{i}\omega)\right) = 0\,, \tag{62}$$

$$\mathrm{Im}\left(D_{\text{char}}(\mathrm{i}\omega)\right) = 0\,, \tag{63}$$

where i is the imaginary unit. The stability boundaries can be analyzed numerically, e.g., with the help of the *Multidimensional Bisection Method* [1]. Namely, the angular frequency ω is swept, while Eqs. (62)-(63) are solved for a range of control gains $K^s_{p\varphi}$ and $K^s_{d\varphi}$. As a result, the stability boundaries are obtained, which can correspond to static ($\omega = 0$) and dynamic ($\omega > 0$) loss of stability.

The stability boundaries of the linearized system are shown with solid black curves in Fig. 4(b), in the plane of control gains $K^s_{p\varphi}$ and $K^s_{d\varphi}$ and for feedback delay $\tau = 0.01$ s.

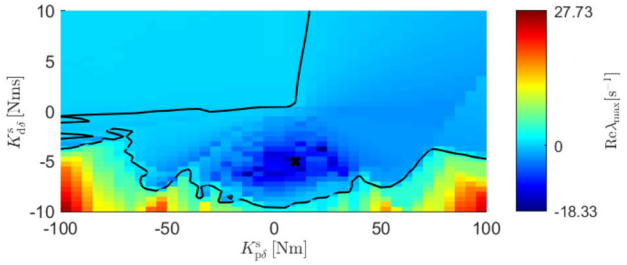

Fig. 5 Stabilizability plot: the real part of the rightmost characteristic root $\mathrm{Re}\lambda_{\max}$ for lower-level control gain pairs $(K^{\mathrm{s}}_{\mathrm{p}\delta}, K^{\mathrm{s}}_{\mathrm{d}\delta})$ (color figure online)

The parameters and the lower-level control gains are fixed and the stability boundaries are plotted for angular frequency $\omega \in [0, 125]$ rad/s. One can observe a static stability boundary ($\omega = 0$) at approximately $K^{\mathrm{s}}_{\mathrm{p}\varphi} = -12.23$, see the vertical line. The curve corresponding to dynamic loss of stability is also plotted, together with the direction of increasing angular frequency ω.

However, the stability properties of the different regions of the stability chart cannot be determined unambiguously in all of the possible cases. Therefore, it is convenient to use semi-discretization [8] to obtain the stable regions and confirm the results of the D-subdivision. In Fig. 4(b), the unstable and the stable regions, obtained by semi-discretization, are indicated by white and gray areas, respectively. Inside the stable region, the optimum point is also plotted with a black cross, for which the rightmost characteristic root, denoted by $\lambda_{\max}$, has the smallest real part. Namely, for this control gain setup, the linear system shows the best robustness against perturbations. In the figure, we also plotted the stability boundaries of the delay-free case. As shown, even a small delay significantly reduces the size of the stable domain, which however shifts into the domain that is linearly unstable without delay.

3.1.3 Proper choice of the lower-level control gains

In the previous subsections, the lower-level control gains $K^{\mathrm{s}}_{\mathrm{p}\delta}$ and $K^{\mathrm{s}}_{\mathrm{d}\delta}$ were fixed. However, they were not chosen randomly, but with optimization with the subject of having the smallest real part of the rightmost characteristic root.

For different lower-level control gain pairs $(K^{\mathrm{s}}_{\mathrm{p}\delta}, K^{\mathrm{s}}_{\mathrm{d}\delta})$, stability charts were constructed by semi-discretization in the plane of the higher-level control gains and the optimum points were obtained. Then, a so-called stabilizability plot was constructed, namely the real part of the rightmost characteristic exponent $\mathrm{Re}\lambda_{\max}$, related to the optimum point is plotted in the plane of the lower-level control gains $K^{\mathrm{s}}_{\mathrm{p}\delta}$ and $K^{\mathrm{s}}_{\mathrm{d}\delta}$, see Fig. 5.

Based on the stabilizability plot, one can easily select which lower-level control gains are appropriate to stabilize the vertical position of the e-scooter. We applied a coloring in Fig. 5: dark blue domains refer to the gain setups where the best performance can be achieved with respect to the decay of the vibrations; colors from cyan to red correspond to non-stabilizable regions. The stability boundary is also highlighted by the solid black curve.

Based on these calculations, the optimal lower-level control gain pair is $K^{\mathrm{s}}_{\mathrm{p}\delta} = 10$ Nm and $K^{\mathrm{s}}_{\mathrm{d}\delta} = -5$ Nms, which is also marked in the figure with a black cross. The stability charts are shown for certain lower-level control gain pairs in Fig. 6. As can be seen, the stable region can be either in the first or in the third quadrant. Note that the size of the stable region is not the greatest for the optimal lower-level control gain pair.

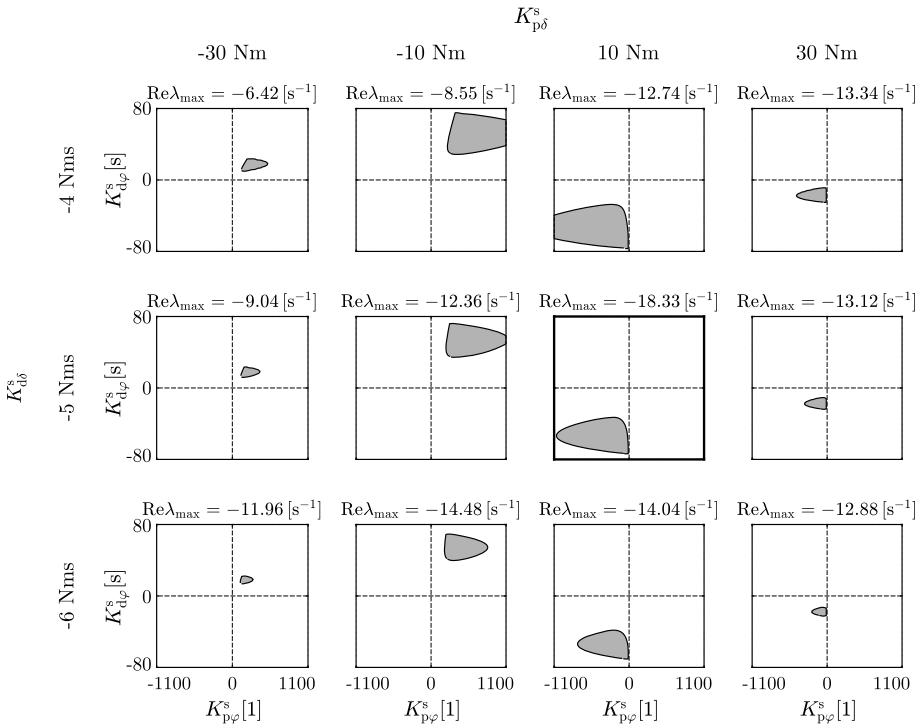

Fig. 6 Stability charts and the real part of the rightmost characteristic roots for certain ($K^{s}_{p\delta}$, $K^{s}_{d\delta}$) lower-level control gain pairs. The borders of the stability chart for the optimal lower-level control gain pair are thickened

3.1.4 The effect of time delay, rake angle, trail and mass distribution on the linear stability

With the proper choice of lower-level control gains for a fixed parameter setup, one can investigate the effect of different parameters on linear stability. According to previous research, the feedback delay τ, the rake angle ε, the trail e and the location x_{KH} of the center of gravity H have significant effects on the linear stability properties. Hence, we analyze their effect by constructing linear stability charts and investigating the real part of the rightmost characteristic roots. In the linear stability charts, the stability boundaries are shown in the plane of the control gains $K^{s}_{p\varphi}$ and $K^{s}_{d\varphi}$. The gray and the white areas correspond to linearly stable and unstable vertical positions, respectively; the different shades of gray relate to different parameter values.

As it can be observed in Fig. 7, the feedback delay influences the linear stability properties significantly. Compared to the delay-free case, marked with a black dashed line in Fig. 7(a), the linearly stable domain is much smaller in the presence of time delay. In addition, the stable domain shrinks considerably with the increasing value of the time delay. Based on Fig. 7(b), the real part of the rightmost characteristic root $\mathrm{Re}\lambda_{max}$ is negative for $\tau < 0.0165$ s. The optimum value for the feedback delay is approximately $\tau = 0.0095$ s.

The linear stability charts are shown for different rake angles and trail values in Fig. 8, for feedback delay $\tau = 0.01$ s. The panel in the middle with thick frame corresponds to the reference setup of [12] with rake angle $\varepsilon = 14.2°$ and trail $e = 0.0281$ m. Linear stability

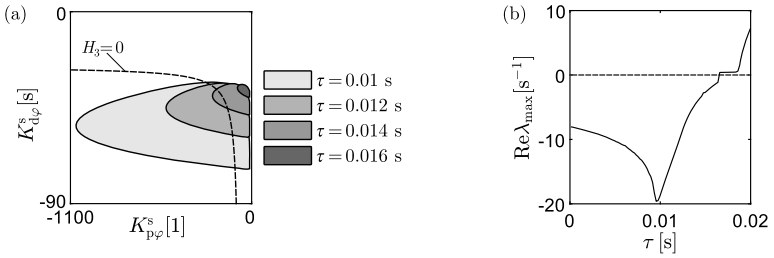

Fig. 7 The effect of the feedback delay on the linear stability for fixed parameters (see Tab. 1) and for fixed lower-level control gains ($K^s_{p\delta} = 10$ Nm and $K^s_{d\delta} = -5$ Nms). (a) Linear stability charts obtained by semi–discretization for four different values of the feedback delay. (b) The real part of the rightmost characteristic roots as a function of the feedback delay

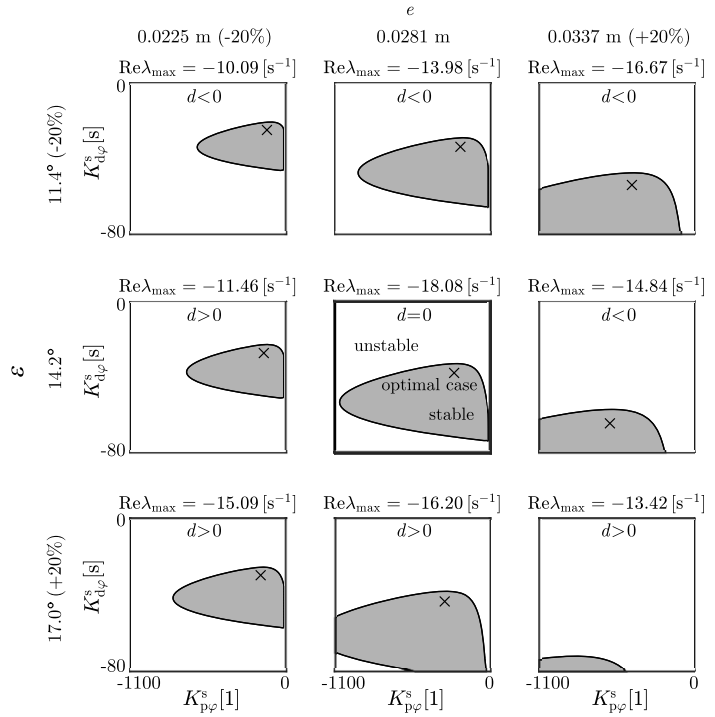

Fig. 8 The effect of the rake angle and the trail on the linear stability. Linear stability charts, the real part of the rightmost characteristic roots, and the value of the fork offset for different values of the rake angle and the trail and for $\tau = 0.01$ s.

charts are drawn for $\pm 20\%$ of the rake angle and the trail in order to investigate the effect of these geometric parameters. The optimal case, in which the real part of the rightmost characteristic root is the smallest, is also marked with a black cross in each stability chart. In addition, the value of the fork offset d is also indicated. As it can be observed, the linearly stable domain, marked with gray, is shifted and expanded by increasing the parameter values

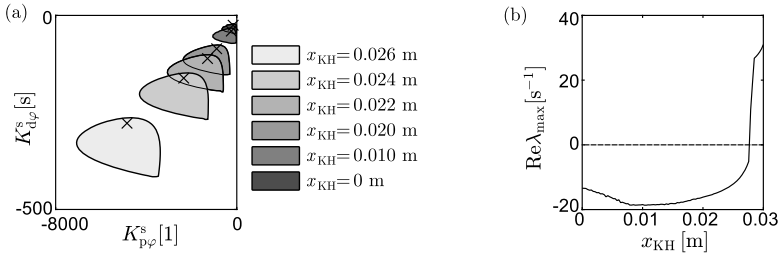

Fig. 9 The effect of the center of gravity of the handlebar on the linear stability for fixed parameters (see Tab. 1) and for fixed lower-level control gains ($K^{\mathrm{s}}_{\mathrm{p}\delta} = 10$ Nm and $K^{\mathrm{s}}_{\mathrm{d}\delta} = -5$ Nms). (a) Linear stability charts obtained by semi-discretization for six different values of the center of gravity of the handlebar. (b) The real part of the rightmost characteristic roots by means of the center of gravity of the handlebar

of the rake angle and the trail. Despite the fact that the stable domain is not the largest for the reference system, the real part of the rightmost characteristic root is the smallest for it.

The feasible value of the feedback delay τ depends on the sensors and actuators in the control loop. In addition, the value for the rake angle ε and the trail e is constrained by the design process of e-scooters. With these limitations, it is convenient to find a parameter, which can be varied independently from the other parameters of the e-scooter and has a significant effect on the linear stability. An easily variable geometric parameter is the center of gravity of the handlebar x_{KH}. As it can be observed in Fig. 9(a), the more the center of gravity of the handlebar afore the steering axis is, the greater the linearly stable region is. However, there is a limit to the parameter value. Namely, based on Fig. 9(b), the vertical position can be stabilized, i.e., the real part of the rightmost characteristic root $\mathrm{Re}\lambda_{\mathrm{max}}$ is negative for $x_{\mathrm{KH}} < 0.0277$ m. The optimum value for the center of gravity of the handlebar is approximately $x_{\mathrm{KH}} = 0.0106$ m.

3.2 Control with driving

As another solution, we try to balance the e-scooter by turning the front wheel into a $\pi/2$ steering angle position and by applying internal driving torque M^{d} on the axis of the front wheel. Thus, our balancing task became similar to the self-balancing problem of segways [15, 41], or to the Furata pendulum balancing problem [37, 38]. Since the steering angle is fixed (i.e., $\delta \equiv \pi/2$), the steering rate is zero (i.e., $\dot{\delta} = 0$). This provides an additional geometric constraint, and the steering angle δ is not a generalized coordinate in this reduced system. However, the kinematic constraints of rolling in Eq. (30) still hold after deleting the fifth column of the coefficient matrix (31). Namely, only two pseudo velocities are required, and the equations of motion of the reduced system can be derived based on Sect. 2.5. For this case, let us choose $\sigma_1 = \dot{\varphi}$ and $\sigma_2 = \dot{\phi}_{\mathrm{f}}$. The vector of state variables is now

$$\mathbf{x} = \begin{bmatrix} \varphi & \phi_{\mathrm{f}} \end{bmatrix}^{\mathrm{T}} . \tag{64}$$

In order to preserve the symmetry of the system, we assume that the center of gravity of the handlebar is on the axis of the handlebar ($x_{\mathrm{KH}} = 0$) and we consider zero fork offset ($d = 0$). Based on Eq. (1), the trail can be calculated for this case as

$$e = R \tan \varepsilon . \tag{65}$$

The nonlinear equations are linearized around the steady state $\mathbf{x}(t) \equiv \mathbf{0}$, namely

$$\varphi(t) \equiv \varphi_0 = 0\,, \tag{66}$$

$$\phi_{\mathrm{f}}(t) \equiv \phi_{\mathrm{f},0} = 0\,. \tag{67}$$

We again approximate the pitch angle with a second-degree expression in order to simplify the calculations of the linearized equations of motion:

$$\vartheta = c_0 + c_2\varphi^2 + \text{h.o.t.}\,, \tag{68}$$

where

$$c_0 =: \vartheta_0 = \arccos\frac{R^2\cos\varepsilon + (R\sin\varepsilon + p)\sqrt{2Rp\sin\varepsilon + p^2}}{R^2 + 2Rp\sin\varepsilon + p^2}, \tag{69}$$

$$c_2 = -\frac{1}{2}\frac{R + R\sin(\varepsilon - \vartheta_0)\tan(\varepsilon - \vartheta_0) - p\sin\vartheta_0}{R\sin(\varepsilon - \vartheta_0) + p\cos\vartheta_0}\,. \tag{70}$$

In order to verify our approximation, the relation between the lean and the pitch angles is shown in Fig. 3(c). The black curve depicts the section at $\delta = \pi/2$ of the surface corresponding to the geometric constraint (25). The red curve shows the approximation (68) between the lean and the pitch angles. As it can be observed, the approximation is precise in case of small lean angles.

The linearized equations of motion can be written similarly as in Eq. (48) with $\mathbf{Q}(t) = \begin{bmatrix}0 & M^{\mathrm{d}}\end{bmatrix}^{\mathrm{T}}$. The mass and the stiffness matrices are given numerically for the parameters of Table 1 in Appendix B. Note that ϕ_{f} is a cyclic coordinate of the open-loop system.

Again, as a first approach, we use a cascade controller. Namely, a higher-level controller calculates the desired front wheel angle as

$$\phi_{\mathrm{f,des}} = -K^{\mathrm{d}}_{\mathrm{p}\varphi}\varphi(t-\tau) - K^{\mathrm{d}}_{\mathrm{d}\varphi}\dot{\varphi}(t-\tau)\,, \tag{71}$$

where τ is the feedback delay in the controller, $K^{\mathrm{d}}_{\mathrm{p}\varphi}$ and $K^{\mathrm{d}}_{\mathrm{d}\varphi}$ are proportional gains for the lean angle and lean rate, respectively. The internal driving torque M^{d} is created by a lower-level control as

$$M^{\mathrm{d}} = -K^{\mathrm{d}}_{\mathrm{p}\phi_{\mathrm{f}}}\left(\phi_{\mathrm{f}}(t) - \phi_{\mathrm{f,des}}\right) - K^{\mathrm{d}}_{\mathrm{d}\phi_{\mathrm{f}}}\dot{\phi}_{\mathrm{f}}(t)\,, \tag{72}$$

where $K^{\mathrm{d}}_{\mathrm{p}\phi_{\mathrm{f}}}$ and $K^{\mathrm{d}}_{\mathrm{d}\phi_{\mathrm{f}}}$ are proportional gains for the front wheel angle and front wheel rate, respectively. We again assume that the time delay in the lower-level controller is negligible compared to the time delay in the higher-level controller.

By applying the control laws described in Eqs. (71)–(72), the vector of generalized forces can be written similarly as in Eq. (51) with the matrices

$$\mathbf{D} = \begin{bmatrix}0 & 0\\ 0 & -K^{\mathrm{d}}_{\mathrm{d}\phi_{\mathrm{f}}}\end{bmatrix}, \quad \mathbf{P} = \begin{bmatrix}0 & 0\\ 0 & -K^{\mathrm{d}}_{\mathrm{p}\phi_{\mathrm{f}}}\end{bmatrix}, \tag{73}$$

$$\mathbf{D}_\tau = \begin{bmatrix}0 & 0\\ -K^{\mathrm{d}}_{\mathrm{p}\phi_{\mathrm{f}}}K^{\mathrm{d}}_{\mathrm{d}\varphi} & 0\end{bmatrix}, \quad \mathbf{P}_\tau = \begin{bmatrix}0 & 0\\ -K^{\mathrm{d}}_{\mathrm{p}\phi_{\mathrm{f}}}K^{\mathrm{d}}_{\mathrm{p}\varphi} & 0\end{bmatrix}. \tag{74}$$

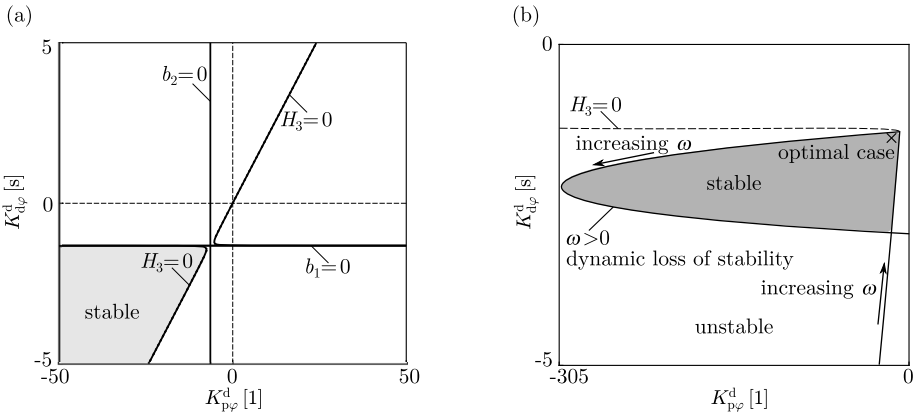

Fig. 10 Stability boundaries and the stable region for fixed parameters of Tab. 1 and for fixed lower-level control gains: $K^{\mathrm{d}}_{\mathrm{p}\phi_{\mathrm{f}}} = -145$ Nm and $K^{\mathrm{d}}_{\mathrm{d}\phi_{\mathrm{f}}} = -30$ Nms. (a) For the non-delayed controller ($\tau = 0$) and (b) for feedback delay $\tau = 0.001$ s.

3.2.1 Control with driving without time delay

By considering zero feedback delay, i.e., $\tau = 0$, the stability boundaries can be analyzed analytically. In this case, for parameter values of Table 1, the coefficients of the characteristic polynomial $D_{\mathrm{char}}(\lambda) = 0$ are

$$b_0 = \det \mathbf{M}\,, \tag{75}$$

$$b_1 = 1.9041 K^{\mathrm{d}}_{\mathrm{d}\phi_{\mathrm{f}}} + 0.29862 K^{\mathrm{d}}_{\mathrm{d}\varphi} K^{\mathrm{d}}_{\mathrm{p}\phi_{\mathrm{f}}}\,, \tag{76}$$

$$b_2 = -3.5433 + 1.9041 K^{\mathrm{d}}_{\mathrm{p}\phi_{\mathrm{f}}} + 0.29862 K^{\mathrm{d}}_{\mathrm{p}\varphi} K^{\mathrm{d}}_{\mathrm{p}\phi_{\mathrm{f}}}\,, \tag{77}$$

$$b_3 = -35.248 K^{\mathrm{d}}_{\mathrm{d}\phi_{\mathrm{f}}}\,, \tag{78}$$

$$b_4 = -35.248 K^{\mathrm{d}}_{\mathrm{p}\phi_{\mathrm{f}}}\,. \tag{79}$$

The Routh–Hurwitz criteria are then the following. The criterion $b_0 > 0$ is always fulfilled, since the determinant of the mass matrix is always positive. The criteria $b_3 > 0$ and $b_4 > 0$ restrict the lower-level control gains to negative values. Namely, the criterion $b_3 > 0$ implies that $K^{\mathrm{d}}_{\mathrm{d}\phi_{\mathrm{f}}} < 0$ and the criterion $b_4 > 0$ corresponds to $K^{\mathrm{d}}_{\mathrm{p}\phi_{\mathrm{f}}} < 0$. The criterion $b_1 > 0$ defines a maximum value for the derivative control gain $K^{\mathrm{d}}_{\mathrm{d}\varphi}$. Similarly, the criterion $b_2 > 0$ defines a maximum value for the proportional control gain $K^{\mathrm{d}}_{\mathrm{p}\varphi}$. All in all, the stable domain is restricted to a quarter-plane.

In the linear stability chart of Fig. 10(a), the stability boundaries and the stable region are plotted in the plane of control gains $K^{\mathrm{d}}_{\mathrm{p}\varphi}$ and $K^{\mathrm{d}}_{\mathrm{d}\varphi}$. The lower-level control gains are fixed to $K^{\mathrm{d}}_{\mathrm{p}\phi_{\mathrm{f}}} = -145$ Nm and $K^{\mathrm{d}}_{\mathrm{d}\phi_{\mathrm{f}}} = -30$ Nms based on detailed analysis explained later in Sect. 3.2.3. The curve corresponding to $H_3 = 0$ is also marked in the figure. It can be shown that the stable region is the gray-shaded area.

3.2.2 Control with driving with time delay

In the presence of feedback delay, the linear stability charts are constructed with the D-subdivision method and with semi-discretization. The stability boundaries of the linearized

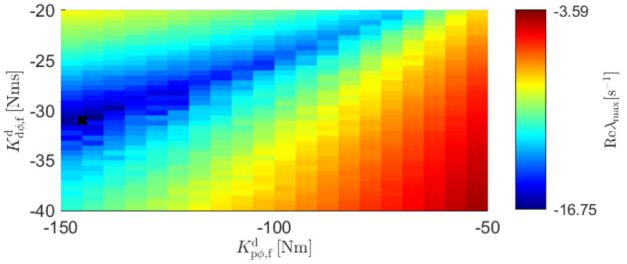

Fig. 11 Stabilizability plot: the real part of the rightmost characteristic root $\mathrm{Re}\lambda_{\max}$ for lower-level control gain pairs $(K^{\mathrm{d}}_{\mathrm{p}\phi_{\mathrm{f}}}, K^{\mathrm{d}}_{\mathrm{d}\phi_{\mathrm{f}}})$ (color figure online)

system are shown with solid black curves in Fig. 10(b), in the plane of the control gains for feedback delay $\tau = 0.001$ s. The parameters and the lower-level control gains are fixed and the stability boundaries are plotted for the angular frequency $\omega \in [0, 1100]$ rad/s. In the figure, the unstable and the stable regions, obtained by semi-discretization, are indicated by white and gray areas, respectively. Inside the stable region, the optimum point is also plotted with a black cross. Note that the stable region is much smaller compared to the delay-free case marked with $H_3 = 0$. It is also worth mentioning, that the optimum point is located close to the stability boundary.

3.2.3 Proper choice of the lower-level control gains

The lower-level control gains $K^{\mathrm{d}}_{\mathrm{p}\phi_{\mathrm{f}}}$ and $K^{\mathrm{d}}_{\mathrm{d}\phi_{\mathrm{f}}}$ were chosen based on similar calculations as for the control with steering case. Namely, semi-discretization was performed for lower-level control gain pairs, the characteristic exponents were calculated and the optimum points were obtained. The stabilizability plot can be seen in Fig. 11.

As can be seen in Fig. 11, the real part of the rightmost characteristic root is negative for the whole domain, i.e., the motion is stabilizable for all investigated lower-level control gain pairs. The minimal of $\mathrm{Re}\lambda_{\max}$ corresponds to $K^{\mathrm{d}}_{\mathrm{p}\phi_{\mathrm{f}}} = -145$ Nm and $K^{\mathrm{d}}_{\mathrm{d}\phi_{\mathrm{f}}} = -30$ Nms. This optimal control gain pair is also marked in the figure with a black cross.

3.2.4 The effect of time delay, rake angle and mass distribution on the linear stability

In the case of control with driving, we investigate the effect of the time delay τ, the rake angle ε and the vertical position z_{KH} of center of gravity of the handlebar on the linear stability. In the linear stability charts, the stability boundaries are shown in the plane of the control gains. The gray and the white areas correspond to linearly stable and unstable motion, respectively; the different shades of gray relate to different parameter values.

As can be observed in Fig. 12(a), the linearly stable domain is much smaller in the presence of time delay. In addition, the larger the value of time delay is, the smaller the stable region is. The motion is stabilizable, i.e., the real part of the rightmost characteristic root is negative for $\tau < 0.00175$ s, see Fig. 12(b). The optimum value for the feedback delay is approximately $\tau = 0.0011$ s. All this means, that the critical time delay is much smaller when the control is done by the driving torque than when the steering is used. The very small critical time delay values may correspond to the fact that we used a hierarchical controller in our study. A one-level direct control of the driving torque based on the lean angle/rate and front wheel angle/rate could tolerate a larger time delay, see [7, 19, 41].

For the control with driving case, we considered zero fork offset for the e-scooter. Therefore, according to Eq. (65), the trail depends on the rake angle. Thus, the effect of the rake angle and the trail can only be investigated together. The linear stability charts are shown for

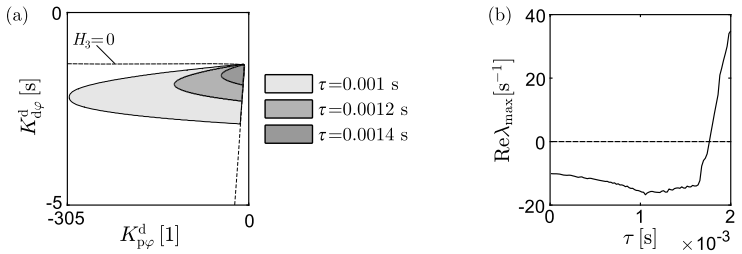

Fig. 12 The effect of the feedback delay on the linear stability for fixed parameters (see Tab. 1) and for fixed lower-level control gains ($K^{\mathrm{d}}_{\mathrm{p}\phi_{\mathrm{f}}} = -145$ Nm and $K^{\mathrm{d}}_{\mathrm{d}\phi_{\mathrm{f}}} = -30$ Nms). (a) Linear stability charts obtained by semi-discretization for three different values of the feedback delay. (b) The real part of the rightmost characteristic roots by means of the feedback delay

Fig. 13 The effect of the rake angle and the trail on the linear stability. Linear stability charts and the real part of the rightmost characteristic roots for different values of the rake angle (thus, for different values of the trail) and for $\tau = 0.001$ s

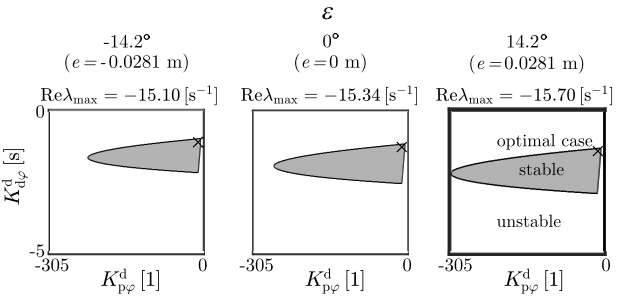

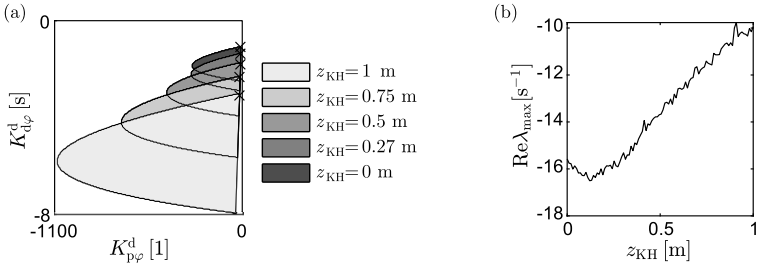

Fig. 14 The effect of the center of gravity of the handlebar on the linear stability for fixed parameters (see Tab. 1) and for fixed lower-level control gains ($K^{\mathrm{d}}_{\mathrm{p}\phi_{\mathrm{f}}} = -145$ Nm and $K^{\mathrm{d}}_{\mathrm{d}\phi_{\mathrm{f}}} = -30$ Nms). (a) Linear stability charts obtained by semi-discretization for five different values of the center of gravity of the handlebar. (b) The real part of the rightmost characteristic roots by means of the center of gravity of the handlebar

different rake angle values in Fig. 13, for feedback delay $\tau = 0.001$ s. On the one hand, the stable region and the real part of the rightmost characteristic root are the largest for $\varepsilon = 14.2°$ and $e = 0.0281$ m (i.e., for the reference parameters). On the other hand, theoretically, there exists a considerable stable region for zero and even negative trail values.

An easily variable geometric parameter is the vertical location z_{KH} of the center of gravity of the handlebar. It can be seen in Fig. 14(a), that the higher the center of gravity of the handlebar, the larger the stable domain. This effect is well-known in the literature, e.g., the analysis of human balancing provides similar results, see [9, 18, 33]. Higher center of gravity

positions allow the use of a larger time delay in the loop. However, the real part of the rightmost characteristic root is smaller for lower center of gravity positions, see Fig. 14(b). The optimum value for the location of the center of gravity is approximately $z_{\mathrm{KH}} = 0.1212$ m.

4 Nonlinear simulations

We designed the controllers for the two different control strategies by means of simplified mechanical models. Namely, we assumed zero rotational speed ($\phi_{\mathrm{f}} \equiv 0$) for the front wheel when the balancing is achieved with steering and we used a fixed steering angle ($\delta \equiv \pi/2$) assumption when the vertical position is stabilized by the driving of the front wheel. However, driving and steering controllers realize these additional geometric constraints in reality.

To check the performance of the control algorithms we designed in Sects. 3.1 and 3.2, we perform nonlinear simulations on the general model described in Sect. 2. In order to gain some knowledge about large amplitude vibrations, we use the nonlinear governing equations of Eq. (37) together with formulas of the generalized velocities $\dot{q}_k$ determined by solving of Eq. (36). Thus, the state variables form the following vector:

$$\mathbf{x}_{\mathrm{full}} = \begin{bmatrix} \mathbf{q} & \sigma \end{bmatrix}^{\mathrm{T}} = \begin{bmatrix} X & Y & \psi & \varphi & \delta & \phi_{\mathrm{f}} & \phi_{\mathrm{r}} & \sigma_1 & \sigma_2 & \sigma_3 \end{bmatrix}^{\mathrm{T}}. \tag{80}$$

4.1 Nonlinear simulations: control with steering

For the sake of simplicity, Explicit Euler method was used with fixed time step of $5 \cdot 10^{-5}$ s. The initial condition was $\mathbf{x}_{\mathrm{full}}(t) = \mathbf{0}$ for $t \in [-\tau, 0)$ and

$$\mathbf{x}_{\mathrm{full}}(0) = \begin{bmatrix} 0 & 0 & 0 & 0 & 0 & 0 & 0 & \omega_0 & 0 & 0 \end{bmatrix}^{\mathrm{T}}, \tag{81}$$

where $\omega_0 := \dot{\varphi}(0) = 0.025$ rad/s, namely, an impact-like perturbation was applied via the non-zero lean rate of the e-scooter. The desired steering angle and the internal steering torque were calculated as in Eqs. (49)–(50). Without fixing the front wheel to the handlebar and fork assembly according to Sect. 3.2, driving torque $M^{\mathrm{d}} = -K^{\mathrm{s}}_{\mathrm{p}\phi_{\mathrm{f}}}\phi_{\mathrm{f}}(t) - K^{\mathrm{s}}_{\mathrm{d}\phi_{\mathrm{f}}}\dot{\phi}_{\mathrm{f}}(t)$ was also applied to force the front wheel to $\phi_{\mathrm{f}}(t) = 0$ and $\dot{\phi}_{\mathrm{f}}(t) = 0$.

The results of the simulation are shown in Fig. 15. Even though the longitudinal and lateral movement and the yaw motion of the e-scooter are not controlled, the positions (X and Y) and the yaw angle (ψ) remain small. More importantly, the lean angle is also small, while the steering angle exceeds 0.2 rad. Since the longitudinal speed of the e-scooter is not prescribed in this general model, the front wheel also moves, but the controller stabilizes it at the desired zero position. The lean, steering and front wheel rates decay in time. The steering controller designed based on our linear analysis performs well also in the case of large steering angles.

4.2 Nonlinear simulations: control with driving

The same numerical method was used with a time step of $5 \cdot 10^{-5}$ s for this simulation. The initial condition was $\mathbf{x}_{\mathrm{full}}(t) = \begin{bmatrix} 0 & 0 & 0 & \varphi_0 & \pi/2 & 0 & 0 & 0 & 0 & 0 \end{bmatrix}^{\mathrm{T}}$ for $t \in [-\tau, 0)$ and the same impact-like perturbation was applied for the lean rate of the e-scooter

$$\mathbf{x}_{\mathrm{full}}(0) = \begin{bmatrix} 0 & 0 & 0 & \varphi_0 & \pi/2 & 0 & 0 & \omega_0 & 0 & 0 \end{bmatrix}^{\mathrm{T}}, \tag{82}$$

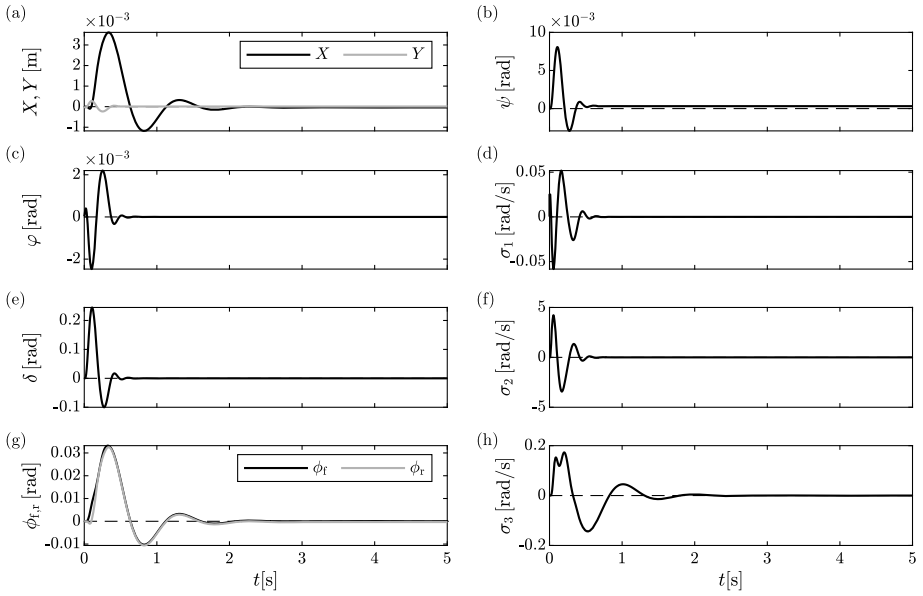

Fig. 15 Nonlinear simulation results for the control with steering case: the time graphs for the state variables. Parameter values as in Tab. 1, $\tau = 0.01$ s, control gains: $K^{\mathrm{s}}_{\mathrm{p}\delta} = 10$ Nm, $K^{\mathrm{s}}_{\mathrm{d}\delta} = -5$ Nms, $K^{\mathrm{s}}_{\mathrm{p}\varphi} = -252.53$, $K^{\mathrm{s}}_{\mathrm{d}\varphi} = -37.47$ s, $K^{\mathrm{s}}_{\mathrm{p}\phi_{\mathrm{f}}} = 10$ Nm, $K^{\mathrm{s}}_{\mathrm{d}\phi_{\mathrm{f}}} = 1$ Nms.

with $\varphi_0 = 9.244 \cdot 10^{-3}$ rad and $\omega_0 := \dot{\varphi}(0) = 0.025$ rad/s. The desired front wheel angle and the internal driving torque were calculated as in Eqs. (71)–(72). Since the steering angle is not prescribed in this general model by any constraint, the steering torque $M^{\mathrm{s}} = -K^{\mathrm{d}}_{\mathrm{p}\delta}(\delta(t) - \pi/2) - K^{\mathrm{d}}_{\mathrm{d}\delta}\dot{\delta}(t)$ was applied to hold $\delta(t) = \pi/2$ and $\dot{\delta}(t) = 0$. Another difference to the mechanical model used in Sect. 3.2 for the controller design is related to the center of gravity of the handlebar. Namely, we consider non-zero value for the longitudinal position x_{KH} of the center of gravity H, which in case of $\delta = \pi/2$ results in a non-zero equilibrium for the lean angle (i.e., $\varphi_0 \neq 0$). Based on this, we modified the reference lean angle value of higher-level control law (71) in simulations. The results of the nonlinear simulation are shown in Fig. 16. As it can be seen, the longitudinal and lateral positions and the yaw angle remain small, even though these are not controlled. As it can be observed in Fig. 16(c), at the end of the simulation, the lean angle converges to the steady-state φ_0. The lean, steering and front wheel rates decay in time. Thus, the designed controller performs exactly as it is proposed by our linear stability analysis.

4.3 Nonlinear simulations: switch from control with steering to control with driving

To verify the feasibility of switching between the different control strategies, we also run a simulation where we suddenly change from the steering control to the driving one. The critical time delay was $\tau = 0.001$ s for the control with driving case, hence simulations are run with the control gains of the linear subsystems of Sects. 3.1 and 3.2 and $\tau = 0.001$ s. The simulation results are shown in Fig. 17. As can be seen, the switch occurs at $t = 5$ s. The vertical position is stabilized by the controllers and the transient caused by the switch is limited both in time and vibration amplitudes.

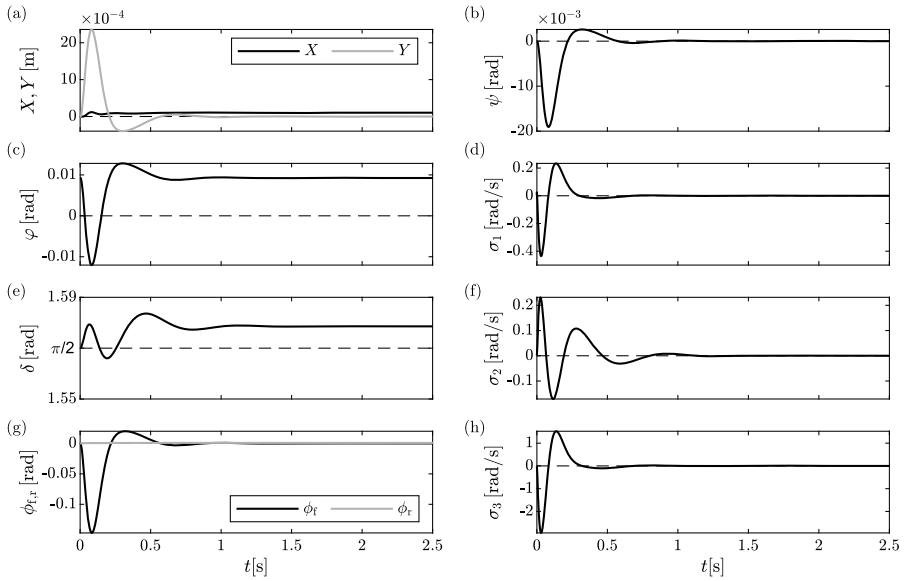

Fig. 16 Nonlinear simulation results for the control with driving case: the time graphs for the state variables. Parameter values as in Tab. 1, $\tau = 0.001$ s, control gains: $K^{\mathrm{d}}_{\mathrm{p}\phi_{\mathrm{f}}} = -145$ Nm, $K^{\mathrm{d}}_{\mathrm{d}\phi_{\mathrm{f}}} = -30$ Nms, $K^{\mathrm{d}}_{\mathrm{p}\varphi} = -7.99$, $K^{\mathrm{d}}_{\mathrm{d}\varphi} = -1.39$ s, $K^{\mathrm{d}}_{\mathrm{p}\delta} = 10$ Nm, $K^{\mathrm{d}}_{\mathrm{d}\delta} = 1$ Nms.

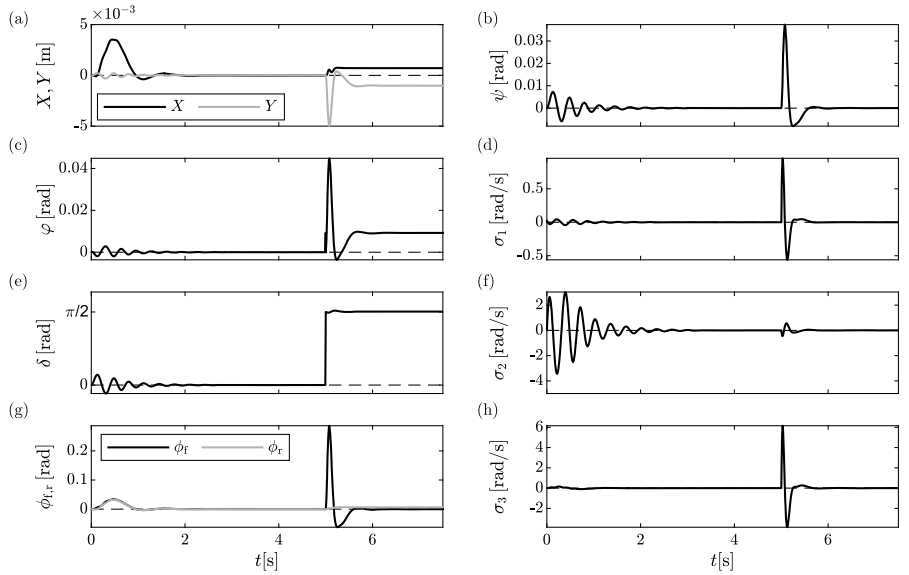

Fig. 17 Nonlinear simulation results for the switch from control with steering to control with driving case: the time graphs for the state variables. Parameter values as in Tab. 1, $\tau = 0.001$ s, control gains for $t < 5$ s: $K^{\mathrm{s}}_{\mathrm{p}\delta} = 10$ Nm, $K^{\mathrm{s}}_{\mathrm{d}\delta} = -5$ Nms, $K^{\mathrm{s}}_{\mathrm{p}\varphi} = -252.53$, $K^{\mathrm{s}}_{\mathrm{d}\varphi} = -37.47$ s, $K^{\mathrm{s}}_{\mathrm{p}\phi_{\mathrm{f}}} = 10$ Nm, $K^{\mathrm{s}}_{\mathrm{d}\phi_{\mathrm{f}}} = 1$ Nms, control gains for $t \geq 5$ s: $K^{\mathrm{d}}_{\mathrm{p}\phi_{\mathrm{f}}} = -145$ Nm, $K^{\mathrm{d}}_{\mathrm{d}\phi_{\mathrm{f}}} = -30$ Nms, $K^{\mathrm{d}}_{\mathrm{p}\varphi} = -7.99$, $K^{\mathrm{d}}_{\mathrm{d}\varphi} = -1.39$ s, $K^{\mathrm{d}}_{\mathrm{p}\delta} = 10$ Nm, $K^{\mathrm{d}}_{\mathrm{d}\delta} = 1$ Nms.

5 Conclusions and discussion

In this study, we designed two control algorithms to balance a riderless self-driven electric scooter at zero forward speed. First, the e-scooter was balanced by using the steering mechanism (control with steering). Next, the front wheel was turned to the steering angle $\pi/2$, and driving torque was applied on the front wheel (control with driving) to stabilize the vertical position. Simple linear state feedback controllers were implemented, and a careful analysis was accomplished with respect to the effect of the time delay and geometric parameters of the e-scooter.

Thanks to the optimization process, optimal control gains of the hierarchical controllers were selected. The mass distribution of the handlebar and fork assembly was identified as a key parameter by which the performance of the controllers can be tuned easily. Hence, other geometric parameters (e.g. trail, rake angle) can be chosen with respect to another aspect (like human handling). Nonlinear numerical simulations confirmed the effectiveness of the proposed control algorithms. The feasibility of switching between the different controllers was also verified. In future work, the validation of the theoretical results of this study will be accomplished using a prototype self-driven e-scooter.

Appendix A

By considering the parameters given in Table 1 and the linearized equations of motion for the control with steering case, the mass and the stiffness matrices read

$$\mathbf{M} = \begin{bmatrix} 1.80613 & 0.0350729 \\ 0.0350729 & 0.111656 \end{bmatrix} \mathrm{kg\,m^2}, \tag{83}$$

$$\mathbf{K} = \begin{bmatrix} -38.79 & 3.01123 \\ 3.01123 & -0.738676 \end{bmatrix} \mathrm{Nm}. \tag{84}$$

Appendix B

By considering the parameters given in Table 1 and the linearized equations of motion for the control with driving case, the mass and the stiffness matrices read

$$\mathbf{M} = \begin{bmatrix} 1.90414 & -0.298616 \\ -0.298616 & 0.100526 \end{bmatrix} \mathrm{kg\,m^2}, \tag{85}$$

$$\mathbf{K} = \begin{bmatrix} -27.2847 & 0 \\ 0 & 0 \end{bmatrix} \mathrm{Nm}. \tag{86}$$

Acknowledgements The authors thank the reviewers for their detailed and essential comments on the manuscript.

Author contributions H.Z.H. carried out the investigation, wrote the main manuscript text and prepared Figs. 3-17. D.T. had the lead role in conceptualization, supervised the work and prepared Figs. 1-2. All authors reviewed the manuscript.

Funding Open access funding provided by Budapest University of Technology and Economics. The research has been supported by the HUN-REN Hungarian Research Network and by the National Research, Development, and Innovation Office under grant no. NKFI-146201 and under grant no. 2020-1.2.4-TET-IPARI-2021-00012. H.Z.H. is supported by the UNKP-22-3-II-BME-101 New National Excellence Program of the Ministry for Innovation and Technology from the source of the National Research, Development and Innovation Fund. D.T. is supported by the Janos Bolyai Research Scholarship of the Hungarian Academy of Sciences.

Declarations

Competing interests The authors declare no competing interests.

References

1. Bachrathy, D., Stepan, G.: Bisection method in higher dimensions and the efficiency number. Period. Polytech., Mech. Eng. **56**(2), 81–86 (2012). https://doi.org/10.3311/pp.me.2012-2.01
2. Basu-Mandal, P., Chatterjee, A., Papadopoulos, J.: Hands-free circular motions of a benchmark bicycle. Proc. R. Soc. A, Math. Phys. Eng. Sci. **463**, 1983–2003 (2007). https://doi.org/10.1098/rspa.2007.1849
3. Cao, X., Bui, D.C., Takacs, D., Orosz, G.: Autonomous unicycle: modeling, dynamics, and control. Multibody Syst. Dyn. (2023). https://doi.org/10.1007/s11044-023-09923-7
4. Chen, C.K., Dao, T.S.: Fuzzy control for equilibrium and roll-angle tracking of an unmanned bicycle. Multibody Syst. Dyn. **15**(4), 321–346 (2006). https://doi.org/10.1007/s11044-006-9013-7
5. Cossalter, V.: Motorcycle Dynamics. Race Dynamics (2002)
6. Edelmann, J., Haudum, M., Plöchl, M.: Bicycle rider control modelling for path tracking. IFAC-PapersOnLine **48**(1), 55–60 (2015). https://doi.org/10.1016/j.ifacol.2015.05.070
7. Horvath, H.Z., Takacs, D.: Balancing standstill motorcycles by steering control with feedback delay. In: The Evolving Scholar - BMD 2023, 5th edn. (2023). https://doi.org/10.59490/647daeb569d559aa327d02f6
8. Insperger, T., Stepan, G.: Semi-Discretization for Time-Delay Systems: Stability and Engineering Applications, vol. 178. Springer, New York (2011). https://doi.org/10.1007/978-1-4614-0335-7_3
9. Insperger, T., Milton, J., Stepan, G.: Acceleration feedback improves balancing against reflex delay. J. R. Soc. Interface **10**, 20120763 (2013). https://doi.org/10.1098/rsif.2012.0763
10. Kane, T.R., Levinson, D.A.: Dynamics: Theory and Applications. McGraw-Hill Book Company, New York (1985)
11. Klinger, F., Nusime, J., Edelmann, J., Plöchl, M.: Wobble of a racing bicycle with a rider hands on and hands off the handlebar. Veh. Syst. Dyn. **52**, 51–68 (2014). https://doi.org/10.1080/00423114.2013.877592
12. Klinger, F., Klinger, M., Edelmann, J., Plöchl, M.: Electric scooter dynamics – from a vehicle safety perspective. In: Orlova, A., Cole, D. (eds.) Advances in Dynamics of Vehicles on Roads and Tracks II, pp. 1102–1112. Springer, Cham (2022). https://doi.org/10.1007/978-3-031-07305-2_102
13. Kooijman, J.D.G., Schwab, A.L., Meijaard, J.P.: Experimental validation of a model of an uncontrolled bicycle. Multibody Syst. Dyn. **19**, 115–132 (2008). https://doi.org/10.1007/s11044-007-9050-x
14. Kooijman, J.D.G., Meijaard, J.P., Papadopoulos, J.M., Ruina, A., Schwab, A.L.: A bicycle can be self-stable without gyroscopic or caster effects. Science **332**(6027), 339–342 (2011). https://doi.org/10.1126/science.1201959
15. Liang, S., Wang, Z., Stepan, G.: Motion control of a two-wheeled inverted pendulum with uncertain rolling resistance and angle constraint based on slow-fast dynamics. Nonlinear Dyn. **104**(3), 2185–2199 (2021). https://doi.org/10.1007/s11071-021-06439-7
16. Lipp, G.M.: Single-track vehicle dynamics and stability. Ph.D. thesis, Duke University (2014)

17. Meijaard, J.P., Papadopoulos, J.M., Ruina, A., Schwab, A.L.: Linearized dynamics equations for the balanceand steer of a bicycle: a benchmark and review. Proc. R. Soc. A **463**, 1955–1982 (2007). https://doi.org/10.1098/rspa.2007.1857
18. Milton, J., Insperger, T., Stepan, G.: Human balance control: dead zones, intermittency, and micro-chaos. In: Ohira, T., Uzawa, T. (eds.) Mathematical Approaches to Biological Systems, pp. 1–28. Springer, Japan (2015). https://doi.org/10.1007/978-4-431-55444-8_1
19. Molnar, T.G., Kiss, A.K., Ames, A.D., Orosz, G.: Safety-critical control with input delay in dynamic environment. IEEE Trans. Control Syst. Technol. **31**(4), 1507–1520 (2023). https://doi.org/10.1109/TCST.2022.3227451
20. Moore, J.K.: Human control of a bicycle. Ph.D. thesis, University of California (2012)
21. Moore, J.K., Hubbard, M., Hess, R.A.: An optimal handling bicycle. In: Proceedings of Bicycle and Motorcycle 2016, Symposium on the Dynamics and Control of Single Track Vehicles (2016). https://doi.org/10.6084/M9.FIGSHARE.3806310.V1
22. Passigato, F., Schramm, A., Diermeyer, F., Sorrentino, S., Gordner, A., Felice, A.D.: Identification of lumped stiffness parameters for a motorcycle model in investigating weave and wobble. Multibody Syst. Dyn. **60**, 233–255 (2023). https://doi.org/10.1007/s11044-023-09899-4
23. Paudel, M., Yap, F.F.: Front steering design guidelines formulation for e-scooters considering the influence of sitting and standing riders on self-stability and safety performance. J. Automob. Eng. **235**(9), 2551–2567 (2021). https://doi.org/10.1177/0954407021992176
24. Peterson, D., Hubbard, M.: Analysis of the holonomic constraint in the Whipple bicycle model (P267). In: The Engineering of Sport 7, pp. 623–631. Springer, Paris (2008). https://doi.org/10.1007/978-2-287-09413-2_75
25. Plöchl, M., Edelmann, J., Angrosch, B., Ott, C.: On the wobble mode of a bicycle. Veh. Syst. Dyn. **50**(3), 415–429 (2012). https://doi.org/10.1080/00423114.2011.594164
26. Psiaki, M.L.: Bicycle stability: a mathematical and numerical analysis. Master's thesis, Physics Department, Princeton University (1979)
27. Qin, W.B., Zhang, Y., Takacs, D., Stepan, G., Orosz, G.: Nonholonomic dynamics and control of road vehicles: moving toward automation. Nonlinear Dyn. **110**(3), 1959–2004 (2022). https://doi.org/10.1007/s11071-022-07761-4
28. Schramm, A.E., Sorrentino, S., Felice, A.D.: Nonlinear effects on the self-excited chatter oscillations in motorcycle dynamics, including tyre relaxation. Nonlinear Dyn. **111**(14), 12671–12698 (2023). https://doi.org/10.1007/s11071-023-08571-y
29. Schwab, A.L., Meijaard, J.P., Papadopoulos, J.M.: Benchmark results on the linearized equations of motion of an uncontrolled bicycle. J. Mech. Sci. Technol. **19**(S1), 292–304 (2005). https://doi.org/10.1007/bf02916147
30. Sharp, R.S., Limebeer, D.J.N.: A motorcycle model for stability and control analysis. Multibody Syst. Dyn. **6**, 123–142 (2001). https://doi.org/10.1023/A:1017508214101
31. Sharp, R.S., Watanabe, Y.: Chatter vibrations of high-performance motorcycles. Veh. Syst. Dyn. **51**(3), 393–404 (2013). https://doi.org/10.1080/00423114.2012.727440
32. Sharp, R.S., Evangelou, S., Limebeer, D.J.N.: Advances in the modelling of motorcycle dynamics. Multibody Syst. Dyn. **12**(3), 251–283 (2004). https://doi.org/10.1023/B:MUBO.0000049195.60868.a2
33. Stepan, G.: Delay effects in the human sensory system during balancing. Philos. Trans. R. Soc. A, Math. Phys. Eng. Sci. **367**(1891), 1195–1212 (2009). https://doi.org/10.1098/rsta.2008.0278
34. Tanelli, M., Corno, M., Filippi, P.D., Rossi, S., Savaresi, S., Fabbri, L.: Control-oriented steering dynamics analysis in sport motorcycles: modeling, identification and experiments. IFAC Proc. Vol. **42**(10), 468–473 (2009). https://doi.org/10.3182/20090706-3-FR-2004.00077
35. Tomiati, N., Colombo, A., Magnani, G.: A nonlinear model of bicycle shimmy. Veh. Syst. Dyn. **57**(3), 315–335 (2019). https://doi.org/10.1080/00423114.2018.1465574
36. Tomiati, N., Magnani, G., Marcon, M.: An experimental investigation of the bicycle motion during a hands-on shimmy. Veh. Syst. Dyn. **59**(9), 1443–1459 (2021). https://doi.org/10.1080/00423114.2020.1762902
37. Vizi, M.B., Stepan, G.: Experimental bifurcation diagram of Furuta pendulum. In: ASME 2018 Dynamic Systems and Control Conference, Volume 3: Modeling and Validation; Multi-Agent and Networked Systems; Path Planning and Motion Control; Tracking Control Systems; Unmanned Aerial Vehicles (UAVs) and Application; Unmanned Ground and Aerial Vehicles; Vibration in Mechanical Systems; Vibrations and Control of Systems; Vibrations: Modeling, Analysis, and Control. American Society of Mechanical Engineers (2018). https://doi.org/10.1115/DSCC2018-9030
38. Vizi, M.B., Stepan, G.: Digital stability of the Furuta pendulum based on angle detection. J. Vib. Control **30**(3–4), 588–597 (2024). https://doi.org/10.1177/10775463221148893
39. Whipple, F.J.W.: The stability of the motion of a bicycle. Q. J. Pure Appl. Math. **30**, 312–348 (1899)

40. Xiong, J., Wang, N., Liu, C.: Stability analysis for the Whipple bicycle dynamics. Multibody Syst. Dyn. **48**, 311–335 (2019). https://doi.org/10.1007/s11044-019-09707-y
41. Xu, Q., Stepan, G., Wang, Z.: Balancing a wheeled inverted pendulum with a single accelerometer in the presence of time delay. J. Vib. Control **23**(4), 604–614 (2017). https://doi.org/10.1177/1077546315583400